



# Image potential in scanning transmission electron microscopy

A. Rivacoba<sup>a,\*</sup>, N. Zabala<sup>b,1</sup>, J. Aizpurua<sup>c</sup>

<sup>a</sup>*Materialen Fisika Saila, Kimika Fakultatea, UPV/EHU, 1072 P.K., 20080, Donostia, Spain*

<sup>b</sup>*Elektrika eta Elektronika Saila, Zientzi Fakultatea, UPV/EHU, 644 P.K., 48080, Bilbao, Spain*

<sup>c</sup>*Department of Applied Physics, Chalmers University of Technology, SE-41296, Göteborg, Sweden*

---

## Abstract

In the framework of the classical dielectric theory, the role of the image potential in electron energy loss spectroscopy (EELS) of fast electrons commonly used in scanning transmission electron microscopy travelling near a surface is studied. Relativistic and dispersive corrections are evaluated to establish the range of validity of this theory. The spatial resolution of the EELS technique is discussed for valence and core electron excitations. The effect of the quantal nature of the probe is also discussed. Finally, several problems involving planar surfaces, small particles, cylinders and truncated targets of interest in nanotechnology are studied. © 2000 Elsevier Science Ltd. All rights reserved.

*Keywords:* Image potential; EELS; STEM; Plasmons; Dielectric response; Self-energy; Surface; Small particles

---

## Contents

1. Introduction . . . . .	3
2. Probe–surface interaction: image potential. . . . .	5
3. Excitation of electronic states by extended beam . . . . .	17

---

\* Corresponding author. Donostia International Physics Center (DIPC) and Centro Mixto CSIC-UPV/EHU, Spain.

<sup>1</sup> Donostia International Physics Center (DIPC) and Centro Mixto CSIC-UPV/EHU, Spain

0079-6816/00/\$ - see front matter © 2000 Elsevier Science Ltd. All rights reserved.

PII: S0079-6816(00)00005-8

### Nomenclature

BCM	boundary charge method
EELS	electron energy loss spectroscopy
GF	Green function
MG	Maxwell Garnet
REM	reflection electron microscopy
RHEED	reflection high energy electron diffraction
RPA	random phase approximation
SEM	scanning electron microscopy
STEM	scanning transmission electron microscopy
TEM	transmission electron microscopy

4.	Spatial resolution in valence EELS . . . . .	19
5.	Theoretical approaches to surface–probe interaction . . . . .	22
5.1.	Quantal model: self-energy formalism . . . . .	22
5.2.	Classical approach. . . . .	24
6.	EELS in planar surfaces. . . . .	25
6.1.	Sub-surface sensitivity . . . . .	26
6.2.	EELS in thin films. . . . .	28
6.3.	Reflection in planar surface . . . . .	29
7.	EELS in small particles . . . . .	32
7.1.	Isolated sphere . . . . .	32
7.2.	Supported particles . . . . .	36
7.3.	Hemispherical particles . . . . .	39
7.4.	Relativistic effects in small particles . . . . .	40
7.5.	Many-particle systems . . . . .	42
8.	Cylindrical surfaces . . . . .	46
9.	EELS in complex configurations: truncated nanostructures . . . . .	48
10.	Conclusions . . . . .	52
	Appendix A. . . . .	53
	Appendix B . . . . .	54
	Acknowledgements . . . . .	53
	References . . . . .	60

---

## 1. Introduction

Charged particles have been used, since the first years of this century, to obtain information on the nature and properties of matter. Since Rutherford used  $\alpha$  particles to study the nature of the atomic structure in 1911, many other testing probes have been used to obtain valuable information. Pioneering experiments at the beginning of the last century as Davisson and Germer or Franck–Hertz experiments led to the use of the electron as a testing probe, now widely extended in many techniques in condensed matter physics.

In 1948, Rutherman [1] had already used electrons in transmission mode and obtained electron energy loss spectra in the energy range of a few eV. *Transmission electron microscopy* (TEM) with use of very high energy electrons (100 keV) yields a contrast image when analyzing the electrons transmitted through the sample. Furthermore, the short wave length associated with high energy electrons in *scanning electron microscopy* (SEM) ( $\sim 0.1$  nm for 100 keV electrons) gives high resolution images by scanning the sample with an extremely well focused electron probe and by analysing the back-scattered and secondary emission electrons. The recent development of the *scanning transmission electron microscope* (STEM) has increased the interest in the study of the processes which occur when the scanning electrons are spatially focused and transmitted through the target providing information on a small area of the sample. Sophisticated numerical simulation of the elastic scattering contribution to image contrast is routinely employed in conventional high-resolution electron microscopy of inhomogeneous materials. On the other hand, inelastic scattering processes are a dominant feature in the sample–probe interaction.

Now, when an increasing number of high-resolution microscopes are fitted with energy-loss imaging facilities, a much wider interest in inelastic scattering processes has emerged, with the consequent requirement of theoretical development to interpret them. Spatially resolved *electron energy loss spectroscopy* (EELS) is a powerful tool to study the characteristics and nature of electron excitations in a solid. In this operation mode, the electron beam is extremely well-focused ( $\sim 0.2$  nm) and the energy and weight of the excitations produced in the sample can be studied as a function of the testing position. If, on the other hand, a pre-determined energy loss is selected and the sample is scanned with the focused beam, it is possible to obtain energy filtered maps, which provide information on the area around the sample, where the electron is able to produce excitations of that energy [2–5]. The aim of the theoretical approaches is to relate this information to the composition and microstructure of the sample.

EELS of fast electrons in STEM shows two types of losses, depending on the nature of the initial electron states, which are excited [6] in the sample: core electron excitations that occur at atomically defined energies ( $\omega > 100$  eV) and valence electron collective excitations (up to 50 eV). These last excitations were already theoretically explained by Bohm and Pines [7] in the 1950s. In free electron metals, their typical energy, the so-called *bulk plasmon*,  $\omega_p$ , is directly related to the electronic charge density  $n$ ,  $\omega_p = \sqrt{4\pi n e^2 / m}$  where  $e$  and  $m$  are the

electron charge and mass, respectively. Together with this charge density oscillation in the bulk, Ritchie [8] later predicted the existence of collective excitations associated to electronic charge density oscillations at the surface, which fall below  $\omega_p$ , and are known as *surface plasmons*.

Both spectra have been widely used to investigate the nature and details of the target. The core electron excitations occur when the probe crosses through the target, and provide chemical information about a region of the target of almost atomic size [9]. On the other hand, the valence excitations provide information about surface structures and details with a resolution of the order of several nm. One advantage of valence excitation spectroscopy is that it provides a much strong signal, even for non-penetrating trajectories (the so-called *aloof beam energy loss spectroscopy*) and, therefore, generates less specimen damage [10]. The fact that the time to collect data is small, permits study of chemical changes at the surface in real time [11].

An extensive review of EELS have been provided by Raether [13,14] and Egerton [12]. Raether's book puts emphasis on surface plasmon excitations, while Egerton's pays more attention to the inner-shell excitations for micro-analysis. Both books stress the experimental aspects of EELS. After these classical texts, more recent books by Schattschneider [15,16] have been published. The thirist one gives a general overview of the inelastic processes, introducing the theoretical formulation to describe them.

The aim of the present work is to shed light on the role of the image potential in the inelastic processes, which take place in STEM. We give a theoretical overview of the different models that have been developed in the last two decades to describe the electron energy losses in STEM. We start with the description of the image potential in a planar interface to give account of the surface and bulk contributions to the loss spectra. This simple approach leads to an understanding of the limitations of this model. Then we analyze the quantal effects derived from the spatial width of the beam, and discuss the spatial resolution provided by EELS. After establishing this basis, we describe the techniques used to account for energy losses in targets of increasing complexity. Details on these formalisms are contained in two appendices.

Atomic units ( $\hbar = e^2 = m = 1$ ) are used throughout in expressions, with  $\hbar$  the Planck constant and  $m$  and  $e$  the electron mass and charge, respectively. In these units, the length unit is the Bohr's radius ( $a_0 = 0.529 \text{ \AA}$ ), the velocity unit is the Bohr velocity ( $v_0 = 2.19 \times 10^8 \text{ cm s}^{-1}$ ), the velocity of light is  $c = 137$  and the energy unit is the Hartree (1 Hartree = 27.2 eV). In results, we use mainly eV for energy and nm for distance. In electrodynamical equations, the Gaussian system will be used, where the dielectric function and magnetic susceptibility in vacuum are considered  $\epsilon_0 = \mu_0 = 1$ . In the study of the relativistic corrections, we have always considered non-ferromagnetic media and assume  $\mu = 1$ . In several parts, we use the sign  $|_{\text{traj}}$  to indicate that the corresponding magnitude is evaluated along the trajectory and that it depends only on the variable used to parametrise the probe trajectory. In the case of probes travelling through a medium, we use the notation  $P_{\text{surf}}(\omega)$  for the total contribution of the surface to

the magnitude  $P$ ; note that both surface and bulk excitations are contained in this term.

Most of the theory we present is valid for any local dielectric function and the experimental one should be used to compare the theoretical predictions to the experimental results. Nevertheless, in the theoretical development, we favour the use of the Drude dielectric function; the fact that it involves just one single parameter — the bulk plasmon energy  $\omega_p$  — and leads to sharp and well-defined surface plasmons, makes more direct the interpretation of the theoretical results. Sometimes we refer to these media just as *metallic*.

## 2. Probe–surface interaction: image potential

Let us consider the interaction between a fast probe and a semi-infinite medium bounded by a planar surface. In the frame of classical electrodynamics, the interaction of a fast charge moving near a planar interface is given by the induced potential, i.e., the so-called *image potential*, which problem was first studied by Ritchie [8] and Takimoto [17]. Now we consider the simplest approach to this problem, where a probe of charge  $Z$  is travelling parallel to the surface at a constant distance  $b$  and with constant velocity  $v$ . Because the momentum transfer, associated with the  $\omega$ -component of the induced potential, is of the order of  $\omega v^{-1}$ , a very small magnitude in the range where collective excitations occur (typically smaller than  $10^{-2}$  a.u.), in many situations we can neglect the dispersion effects in the dielectric response function and describe the response of the medium by means of a local dielectric function  $\epsilon(\omega) = \epsilon(q = 0, \omega)$ . Neglecting retardation effects, the total potential is the solution of Poisson equation

$$\nabla^2 \phi(\mathbf{r}, \omega) = -\frac{4\pi}{\epsilon(\omega)} \rho(\mathbf{r}, \omega), \quad (2.1)$$

where  $\rho(\mathbf{r}, \omega)$  stands for the  $\omega$ -component of the charge density. The convention followed for the Fourier transform is in Appendix B. Assuming that the probe is moving along the  $x$ -axis, the charge density is given by:

$$\rho(\mathbf{r}, \omega) = Z \frac{1}{v} e^{i\frac{\omega x}{v}} \delta(y) \delta(z - b). \quad (2.2)$$

The solution of (2.1) can be obtained by the standard electrodynamic techniques (see Appendix B). Then, in the region where the charge is travelling ( $z > 0$ ), the potential can be written as:

$$\begin{aligned} \phi(\mathbf{r}, \omega) = & \\ & -2 \frac{Z}{v} K_0 \left[ \frac{|\omega|}{v} \sqrt{y^2 + (z - b)^2} \right] e^{i\frac{\omega x}{v}} - 2 \frac{Z}{v} \xi(\omega) K_0 \left[ \frac{|\omega|}{v} \sqrt{y^2 + (z + b)^2} \right] e^{i\frac{\omega x}{v}}, \end{aligned} \quad (2.3)$$

where  $x$ ,  $y$  and  $z$  are the cartesian coordinates of  $\mathbf{r}$ ,  $K_0(x)$  stands for the modified Bessel function and  $\zeta(\omega)$  is the planar surface response function defined as:

$$\zeta(\omega) = \frac{\epsilon(\omega) - 1}{\epsilon(\omega) + 1}. \quad (2.4)$$

The first term in (2.3) is the  $\omega$ -component of the Coulomb potential, while the second one is the surface induced potential. This last term can be understood as the  $\omega$ -component of the image potential; the potential created outside the medium by the dynamic image charge, i.e., a charge  $q_{\text{image}}(\omega) = -Z\zeta(\omega)$  placed in front of the probe and inside the medium at a distance  $b$  from the surface. Then, the induced potential is:

$$\phi_{\text{ind}}(\mathbf{r}, t) = -\frac{Z}{\pi v} \int_{-\infty}^{\infty} d\omega \zeta(\omega) K_0 \left[ \frac{|\omega|}{v} \sqrt{y^2 + (z+b)^2} \right] e^{i\frac{\omega x}{v}(x-vt)}. \quad (2.5)$$

Because of the analytic properties of the dielectric function  $\epsilon(\omega)$  [18], the response function satisfies  $\zeta(-\omega) = \zeta^*(\omega)$ , where  $z^*$  stands for the complex conjugate of  $z$ . Therefore, one can write the former expression as an integral over positive values of  $\omega$ :

$$\phi_{\text{ind}}(\mathbf{r}, t) = -\frac{2Z}{\pi v} \int_0^{\infty} d\omega K_0 \left[ \frac{\omega}{v} \sqrt{y^2 + (z+b)^2} \right] \text{Re}\{\zeta(\omega) e^{i\frac{\omega x}{v}(x-vt)}\}, \quad (2.6)$$

where  $\text{Re}\{z\}$  stands for the real part of the complex argument  $z$ . Although (2.6) explicitly exhibits the fact that the field  $\phi_{\text{ind}}(\mathbf{r}, t)$  is real, in many cases it is preferable to handle (2.5).

The Bessel function  $K_0$  is a monotonous decreasing function, with the following limiting values [19]:

$$K_0(x) \sim \begin{cases} \sqrt{\frac{x}{2x}} e^{-x} \left\{ 1 - \frac{1}{8x} + \dots \right\} & x \gg 1 \\ -\ln\left[\frac{x}{2}\right] - 0.5772\dots & x \ll 1 \end{cases}. \quad (2.7)$$

Therefore, in the limit when the argument of the Bessel function is very large, i.e., low velocities or large distances, the main contribution to this integral comes from the low  $\omega$  region. Then, the induced potential can be written as:

$$\phi_{\text{ind}}(\mathbf{r}) = -\zeta(\omega=0) \frac{Z}{\sqrt{(x-vt)^2 + y^2 + (z+b)^2}}, \quad (2.8)$$

where we have made use of the fact that the response function  $\zeta(\omega)$  is real at  $\omega=0$ . Expression (2.8) is the well-known electrostatic limit of the image potential.

In this approach, (2.5) fully describes the interaction between the probe and the interface. From this expression, one can evaluate the *stopping power*  $dE/dx$ ; i.e.,

the energy loss  $dE$  experienced by the probe, when it travels along a path of length  $dx$ . The probe is stopped by the component of the electric force along the motion direction; the stopping power is just this component of the force evaluated at the probe position; i.e.,  $x = vt$ ,  $y = 0$  and  $z = b$ :

$$\frac{dE}{dx} = -Z \frac{\partial \phi_{\text{ind}}}{\partial x} \Big|_{\text{traj}} = -2 \frac{Z^2}{\pi v^2} \int_0^\infty \omega d\omega \text{Im}\{\xi(\omega)\} K_0 \left[ \frac{2\omega b}{v} \right], \quad (2.9)$$

where  $\text{Im}(z)$  stands for the imaginary part of the complex argument  $z$ . The total energy loss given by (2.9) can be interpreted as the result of the excitation of different inelastic processes of energy  $\omega$ , each of them excited with a probability per unit length  $dP(\omega)/dx$ , i.e.,

$$\frac{dE}{dx} = \int_0^\infty \omega d\omega \frac{dP(\omega)}{dx}, \quad (2.10)$$

where:

$$\frac{dP(\omega)}{dx} = 2 \frac{Z^2}{\pi v^2} \text{Im}\{\xi(\omega)\} K_0 \left[ \frac{2\omega b}{v} \right], \quad (2.11)$$

which was first obtained by Echenique and Pendry [20], although it can be derived from a previous work by Takimoto [17].

From (2.9), it is clear that only the imaginary part of the response function  $\xi(\omega)$  is responsible for the inelastic scattering, which is a general feature of this approach. In a metal, the collective surface excitations take place for those values of  $\omega$  for which  $\text{Re}\{\epsilon(\omega)\} \sim -1$ . For a Drude-like metal,  $\epsilon(\omega) = 1 - \omega_p^2/\omega^2$  (Appendix A), the imaginary part of the response function  $\xi(\omega)$  can be simply expressed in terms of a single excitation, the so-called *planar surface plasmon*:

$$\text{Im}\{\xi(\omega)\} = \frac{\pi\omega_s}{2} \delta[\omega - \omega_s], \quad \omega_s = \frac{\omega_p}{\sqrt{2}}. \quad (2.12)$$

Here,  $\omega_s$  is the well-known energy of the surface plasmon which was first introduced by Ritchie [8]. This prediction was confirmed by Powell and Swan [21] in Al and Mg films. Then, the energy loss probability per unit length is:

$$\frac{dP(\omega)}{dx} = \frac{Z^2}{v^2} K_0 \left[ \frac{2\omega b}{v} \right] \omega_s \delta[\omega - \omega_s]. \quad (2.13)$$

In other metallic surfaces, the energy of their surface plasmons (the so-called *modes*) are given by the poles of their corresponding response functions. The modes are the values of  $\omega$  for which the Laplace equation presents non-trivial solutions.

When the probe moves parallel to the surface, but through the medium, the potential can be calculated in a similar way. Then, the induced potential is given by:

$$\begin{aligned} \phi_{\text{ind}}(\mathbf{r}, \omega) = & \\ & 2\frac{Z}{v} \left\{ \frac{1}{\epsilon(\omega)} - 1 \right\} K_0 \left[ \frac{|\omega|}{v} \sqrt{y^2 + (z-b)^2} \right] e^{i\frac{\omega x}{v}} - 2\frac{Z}{v} \zeta(\omega) K_0 \left[ \frac{|\omega|}{v} \sqrt{y^2 + (z+b)^2} \right] e^{i\frac{\omega x}{v}}, \end{aligned} \quad (2.14)$$

where the surface response function  $\zeta(\omega)$  is:

$$\zeta(\omega) = -\frac{1}{\epsilon(\omega)} \frac{\epsilon(\omega) - 1}{\epsilon(\omega) + 1} = \frac{1}{\epsilon(\omega)} + \xi(\omega) - 1. \quad (2.15)$$

In (2.14), the first term is the same as the induced potential created by a probe moving through an unbounded medium of dielectric function  $\epsilon(\omega)$ , while the second one is the contribution of the surface to the induced potential. Proceeding as before, one can calculate from (2.14) the total energy loss probability per unit length [22,23]. It is given by:

$$\frac{dP(\omega)}{dx} = 2\frac{Z^2}{\pi v^2} \text{Im} \left\{ \frac{-1}{\epsilon(\omega)} \right\} \ln \left[ \frac{k_c v}{\omega} \right] + 2\frac{Z^2}{\pi v^2} \text{Im} \left\{ \frac{1}{\epsilon(\omega)} + \xi(\omega) \right\} K_0 \left[ \frac{2\omega b}{v} \right]. \quad (2.16)$$

The first term in (2.16) is the well-known expression for a charge moving in a non-bounded medium; in a metal, it describes the excitations of bulk plasmons. To calculate this bulk contribution, a cut-off  $k_c$  has been used to avoid the contribution of large values of the momentum, which lead to a logarithmic divergence, when a local dielectric response is used [24]. Bulk plasmons are excited — at least in the local dielectric approach — only by probes travelling through the medium. The second term of (2.16) is the surface contribution to the energy loss probability. This contribution is twofold: the term in  $\xi(\omega)$  describes the excitations of surface plasmons, while the term containing  $\epsilon^{-1}$  is a negative correction to the bulk plasmon excitation probability due to the presence of the interface; this term reduces the bulk losses in relation to the case when the probe travels through an unbounded medium, and is the so-called *begrenzung* or *boundary-effect*, first described in films by Ritchie [8] and which appears in other targets for penetrating trajectories of the probe [25]. This effect means that the excitation of surface modes is made at the expense of the bulk modes. For a Drude-like metal, the surface contribution to (2.16) can be written as:

$$\frac{dP_{\text{surf}}(\omega)}{dx} = \frac{Z^2}{v^2} K_0 \left[ \frac{2\omega b}{v} \right] \{ \omega_s \delta[\omega - \omega_s] - \omega_p \delta[\omega - \omega_p] \}, \quad (2.17)$$

which establishes that the reduction of the bulk plasmon excitation probability has exactly the same analytic form, but opposite sign, as that corresponding to surface plasmons. Note that  $\omega_s < \omega_p$ , therefore, the *begrenzung* does not imply that there is a balance in terms of the energy loss; it means that the total energy loss is smaller than that corresponding to an infinite medium. The negative bulk correction is to be balanced by the infinite bulk term, so that the total bulk

plasmon excitation probability is positive. This fact provides a limit to the usefulness of the local dielectric response approach: at impact parameter  $b$  small enough, as to apply the limiting expression (2.7), the bulk plasmon term behaves as:

$$\frac{dP_{\text{bulk}}(\omega)}{dx} \sim 2 \frac{Z^2}{v^2} \text{Im} \left\{ \frac{-1}{\epsilon(\omega)} \right\} \left\{ \ln \left[ \frac{\omega b}{v} \right] + \ln \left[ \frac{k_c v}{\omega} \right] \right\}, \quad (2.18)$$

therefore, (2.16) is only valid for impact parameters  $b > 1/k_c$ , a result implicitly imposed by the cut-off used in the direct bulk term.

In the same way, from (2.5) one can calculate  $F_{\perp}$ , the component of the force normal to the probe trajectory. This force is responsible for the deflection of the trajectory towards the surface:

$$F_{\perp}(b) = -Z \frac{\partial \phi_{\text{ind}}}{\partial z} \Big|_{\text{traj}} = -2 \frac{Z^2}{\pi v^2} \int_0^{\infty} \omega \, d\omega \, \text{Re} \{ \zeta(\omega) \} K_1 \left[ \frac{2\omega b}{v} \right], \quad (2.19)$$

which is valid for any dielectric function and was first obtained by Howie [26]. Eq. (2.19) states that only the real part of the response function is involved in the elastic scattering. The fact that real and imaginary parts of the response function are related to the elastic and inelastic interactions, respectively, is a general result of the non-relativistic theory, valid for any situation, so long as the energy loss is evaluated between probe positions for which the initial and final states of the target are the same, as we will prove in Section 5.2. For a free-electron gas metal, it is possible to integrate (2.19) over  $\omega$  by using the integral representation of the Bessel function [19]. In this way, the normal force can be written in terms of the surface plasmon frequency  $\omega_s$  [27]:

$$\begin{aligned} F_{\perp}(b) &= \frac{Z^2 \omega_s^2}{v^2} \int_0^{\infty} \frac{dt}{\sqrt{1+t^2}} \cos \left[ \frac{2\omega_s b}{v} t \right] \\ &= \frac{Z^2 \omega_s^2}{v^2} \frac{\pi}{2} \left\{ I_1 \left[ \frac{2\omega_s b}{v} \right] - \mathbf{L}_1 \left[ \frac{2\omega_s b}{v} \right] - \frac{2}{\pi} \right\}, \end{aligned} \quad (2.20)$$

where  $I_1$  and  $\mathbf{L}_1$  are the modified first-order Bessel and Struve functions respectively [19]. The limit of this expression for a small impact parameter is:

$$F_{\perp}(b) = -Z \frac{2\omega_s^2}{v^2} \left\{ 1 + 0 \left[ \frac{\omega_s b}{v} \right]^2 + \dots \right\}, \quad b \ll \frac{v}{\omega_s}, \quad (2.21)$$

which indicates that near the interface the normal force remains always finite. Roughly, this finite value is due to the fact that the induced charge density needs a time of about  $\omega_s^{-1}$  to be established and then the image charge is delayed a distance  $\sim v\omega_s^{-1}$  in relation to the actual probe position. This finite result is also valid for more complicated response functions; then the delay should be an

average value of the different excitations, which contribute to the dielectric response function.

For large values of the parameter  $b\omega_s v^{-1}$ , (2.20) leads to the well-known electrostatic limit:

$$F_{\perp}(b) = -Z^2 \frac{1}{4b^2} \left\{ 1 + 0 \left[ \frac{v}{\omega_s b} \right]^2 + \dots \right\}, \quad b \gg \frac{v}{\omega_s}. \quad (2.22)$$

The fact that the force is negative in these expressions means that it is always directed towards the surface when the charge is travelling in vacuum.

Eqs. (2.11), (2.16) and (2.19) exhibit the main features of the inelastic and elastic interactions between probes and surfaces. The expressions for the stopping power have been widely used to study the inelastic interaction of swift charges with large planar surfaces. Many authors have proved that the optical dielectric functions  $\epsilon(\omega)$  explain, in qualitative detail, the surface loss spectra for different materials [28–30,10]. Additionally, the impact parameter dependence given by (2.9) is in good agreement with the experimental results [4,23,31].

An alternative way of tackling the probe–target interaction is through the charge density induced in the target. The polarisation of the medium  $\mathbf{P}$  generates both volume and surface densities. The induced volume density is  $-\nabla \mathbf{P}$  and, consequently, it is proportional to the external charge density in the medium; this charge density takes place only when the probe is moving through a polarisable medium. In this case, the volume charge density leads to the bulk screening factor  $\epsilon^{-1}$ . When the probe travels outside the target, the interaction between probe and target is due only to the potential created by the surface charge density  $\sigma_{\text{ind}}$ . The induced charge density on the surface is the normal component of the polarisation and can be straightforwardly derived from (2.3). It is given by:

$$\sigma_{\text{ind}}(x, y, \omega) = -Z \frac{|\omega|}{\pi v^2} \zeta(\omega) \frac{b}{\sqrt{y^2 + b^2}} K_1 \left[ \frac{|\omega|}{v} \sqrt{y^2 + b^2} \right] e^{i \frac{\omega x}{v}}, \quad (2.23)$$

where  $K_1(x) = -(d/dx)K_0(x)$  is the modified Bessel function of first-order. Its limiting values are given by:

$$K_1(x) \sim \begin{cases} \sqrt{\frac{\pi}{2x}} e^{-x}, & x \gg 1 \\ x^{-1}, & x \ll 1 \end{cases}, \quad (2.24)$$

which means that the induced charge density is spread in the plane over a region of size  $v\omega^{-1}$  in the direction transverse to  $\mathbf{v}$ , while in the direction of  $\mathbf{v}$  it oscillates with a wavelength  $2\pi v\omega^{-1}$ .

Taking into account the behaviour of the Bessel function  $K_0$ , the surface contribution to the energy loss probability in (2.9) diverges as  $\ln\{b\omega v^{-1}\}$  for small values of  $b$ . This effect has not been found experimentally. It is a consequence of the simple local approach used here; this model does not impose any spatial

correlation in the induced charge density, so, at small impact parameters, it tends to pile up an unphysical induced charge density on the interface (2.23).

In a more realistic approach, one should consider that, for small values of  $b$ , large values of the momentum transfer contribute to the dielectric response, hence, one cannot properly neglect the momentum dependence in the dielectric function  $\epsilon(\mathbf{k}, \omega)$ . The effect of the dispersion in the stopping power near a surface has been evaluated for the fast electrons [32–35] and for the general case [36] as well.

Following [35], we study the energy loss experienced by the probe near a dispersive medium in the same situation as above. Now the medium response is described by the Mermin dielectric function [37] (see Appendix A) and the specular reflection model [38] is used to impose the boundary conditions at the interface. In Fig. 1(a), we plot the imaginary part of the surface response function derived for Al as a function of both  $\mathbf{k}$  and  $\omega$ , which decreases for values of the momentum transfer larger than  $0.5k_F$ . This attenuation of the surface response works as an effective cut-off in momentum space and leads to finite values of the surface stopping power, when the impact parameter tends to zero, as shown in Fig. 1(b), which compares both local and dispersive approaches; it proves that the dispersion is only relevant at very small impact parameters  $b \ll v\omega_s^{-1}$ . For larger impact parameters, the main contribution to the potential arises from small momentum transfer, so that both local and non-local descriptions lead to the same results. This conclusion can be generalised for other situations, by stating that local effects are relevant only in situations, where the electron spends most of its flight time at very small distances from the surface. In particular, for penetrating trajectories, the logarithmic divergence of the  $\phi_{\text{ind}}$  near the surface leads to finite values of the energy loss probability, when integrating over the whole trajectory.

A rough evaluation of the error provided by the local approximation for trajectories crossing the interface can be obtained by using the interface parallel path method, which leads to the conclusion that the local approach overestimates the surface plasmon loss in about 5% with respect to the non-local calculation. Even though, in most materials, the description of the excitation spectra provided by the experimental optical function  $\epsilon(\omega)$  is more realistic than that obtained from any theoretical response functions. Several methods to extend the experimental dielectric function  $\epsilon(\omega)$  for large values of  $\mathbf{q}$  have been proposed [39–41]. Some of them are briefly introduced in Appendix A.

Fig. 1 is quite important for discussing the spatial resolution available in valence EELS. Without dispersion, the dependence on  $K_0(2\omega_s b/v)$  shows that  $v/\omega_s$  appears as a scaling factor, but does not really tell much about the resolution, since the Bessel function has a long tail and a very steeply varying part at small  $b$ . With dispersion, as shown by the surface plasmon excitation in Fig. 1, we obtain a clearer picture. Higher spatial resolution can be obtained by selecting only large values of the momentum [35].

The bulk loss probability of Fig. 1(b) presents a similar behaviour; for trajectories inside the metal, the total probability and the surface correction to this

term remain finite near the surface. The small step in the bulk loss probability near the surface has been found experimentally [42,43,5]. Another relevant feature of the non-local approach is that the bulk plasmon field slightly extends outside the medium, whence bulk plasmons can be weakly excited by electrons moving

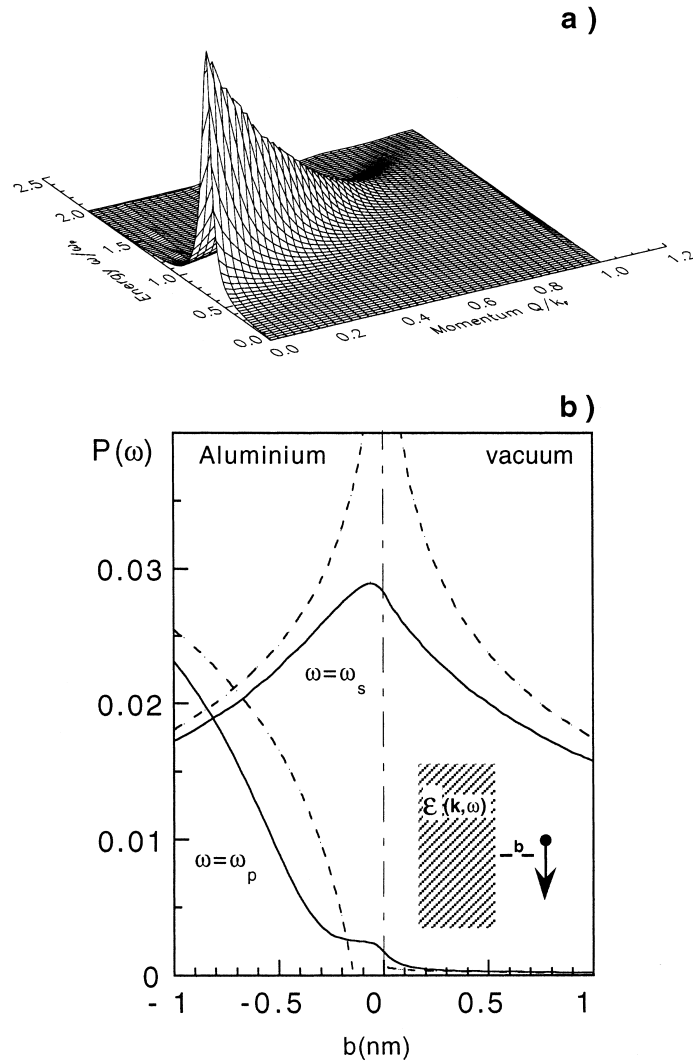


Fig. 1. (a) Imaginary part of surface response function as a function of  $\omega$  (in units of  $\omega_s$ ) and parallel momentum  $q$  (in units of Fermi momentum  $k_F$ ). (b) Comparison of surface and total bulk loss probability as a function of the impact parameter  $b$ , for local (dashed line) and non-local (continuous line) dielectric function (a Mermin dielectric function with  $r_s=2$  and  $\gamma=1$  eV). Geometry is sketched in inset of figure (b). Negative values of  $b$  indicate inner trajectories.

outside the surface, at very small impact parameters. The small tail outside the surface in the local plot is not properly a bulk term: it really comes from the local surface response function  $\xi(\omega)$  when a damped dielectric function is used (A3).

Expression (2.21) has been used by Echenique and Howie [44] to evaluate the deflection angle experienced by the STEM beam passing near a 100 nm long MgO planar surface [29] or Au particles [45], leading to a value which is three orders-of-magnitude smaller than the measured one. Further sophistications of this calculation, taking into account the shape of the target, led to similar values [46,47]. Surface charging has been suggested as a possible reason for the MgO observation, but this is unlikely to be a realistic explanation in the case of the gold particles. More conclusive experiments need to be performed in order to clarify this point.

Another obvious shortcoming of the simple approach presented here derives from neglecting the relativistic effects, which require Maxwell's equations to be solved. The simple fact that the induced charge density and currents are now coupled through a retarded field can change the electromagnetic modes of the target. This effect is independent of the probe velocity and will be studied in the case of spherical particles. Other relativistic effects are related to the velocity of the probe, typically, one half of the velocity of light  $c$  in STEM. In addition to the retardation effect, due to the time the signal takes to reach the surface and to turn back to the probe, some new effects appear: Cherenkov emission becomes possible when the real part of  $\epsilon(\omega)$  becomes large enough:  $\text{Re}\{\epsilon(\omega)\} > (c/v)^2$  and the induced charge density can radiate.

One simple system for studying the retardation effect is that of a planar interface or film [48–51]. Following this last work, we study the case of an electron moving parallel and outside a planar surface at impact parameter  $b$ . This problem provides a simple basis for understanding how the retardation affects the EELS impact parameter dependence. Maxwell's equations can be solved in terms of the Hertz vector [53]. The energy loss probability per unit length is given by:

$$\frac{dP(\omega)}{dx} = 2 \frac{Z^2}{\pi v^2} \int_0^\infty dq_y \frac{e^{-2\mu_0 b}}{\mu_0} \text{Im}\{\lambda_c(\omega, q)\}, \quad (2.25)$$

where  $q_y$  is the component of the momentum in the plane of the surface, normal to the trajectory,  $q^2 = q_y^2 + \omega^2/v^2$  and the retarded loss function  $\lambda_c(\omega, q)$  is given by:

$$\lambda_c(\omega, q) = \frac{1}{\mu + \mu_0} \left\{ \frac{2\mu_0^2(\epsilon - 1)}{\epsilon\mu_0 + \mu} - (1 - \beta^2)(\mu_0 - \mu) \right\}, \quad (2.26)$$

where  $\beta = vc^{-1}$  and

$$\mu = \left[ q_y^2 + \frac{\omega^2}{v^2}(1 - \epsilon\beta^2) \right]^{1/2}, \quad \mu_0 = \left[ q_y^2 + \frac{\omega^2}{v^2}(1 - \beta^2) \right]^{1/2}. \quad (2.27)$$

In the limit  $\beta \rightarrow 0$ , (2.25) yields (2.11). For a metal, the energies of the surface plasmons  $\omega$  are given by the equation  $\epsilon\mu_0 - \mu = 0$ , which leads to:

$$\{2 - \beta^2\} \left(\frac{\omega}{\omega_p}\right)^4 + \left\{2 \left(\frac{qv}{\omega_p}\right)^2 - 1 + \beta^2\right\} \left(\frac{\omega}{\omega_p}\right)^2 - \left(\frac{qv}{\omega_p}\right)^2 = 0, \quad (2.28)$$

therefore, the velocity of the probe introduces a dispersion of the surface plasmon energy, which is significant for high values of  $\beta$ . Fig. 2 shows the modes for different values of the energy. The limiting values of the function  $\omega(q_y)$  are given by:

$$\omega^2 \sim \begin{cases} \frac{\omega_p^2}{2} \frac{1 - \beta^2}{1 - \frac{1}{2}\beta^2}, & q_y \ll \frac{\omega_p}{v}, \\ \frac{\omega_p^2}{2}, & q_y \gg \frac{\omega_p}{v}. \end{cases} \quad (2.29)$$

The dispersion is reflected in the energy loss spectra shown in Fig. 3. For small impact parameters, the main contribution to the integral arises from large values of  $q$ , so the main loss peak occurs near  $\omega_s$ . There is another small peak

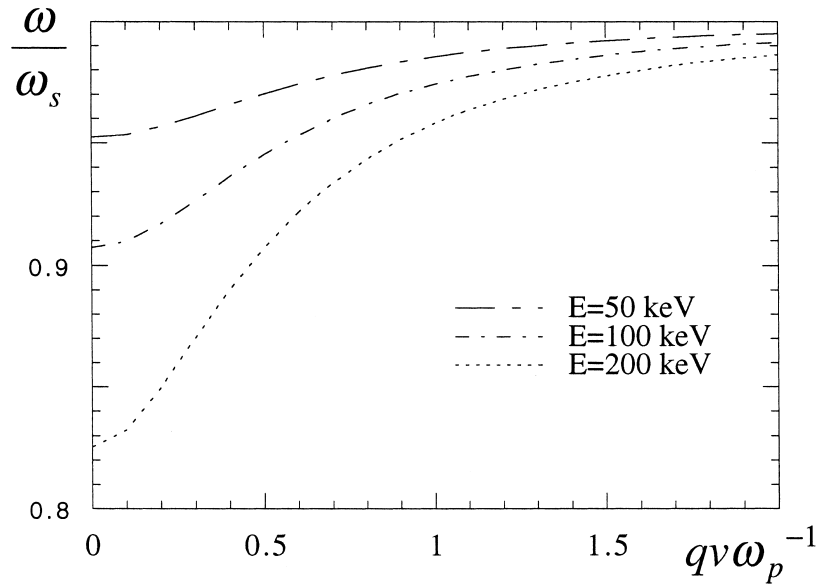


Fig. 2. Retarded dispersion relation in planar interface for three different probe energies. Corresponding  $\beta$  values are 0.41, 0.55 and 0.70, respectively.

corresponding to the low  $q$  contribution, but its intensity is much smaller. The comparison with the non-retarded spectrum shows a reduction in the intensity of the  $\omega_s$  peak, as well as a small red shift of this peak, due to the plasmon dispersion. For a large impact parameter (curve b), the main contribution to the energy loss probability comes from the low  $q$  region, whereby the loss peak is centred at the limit values of  $\omega(q_y)$  for  $q \rightarrow 0$  in (2.29). All the relativistic effects in these spectra derive from just the retardation in the interaction, because in this case there is no Cherenkov emission ( $\epsilon(\omega) < 0$ ) and surface plasmons cannot radiate, since the dispersion curves for both surface plasmons and photons do not

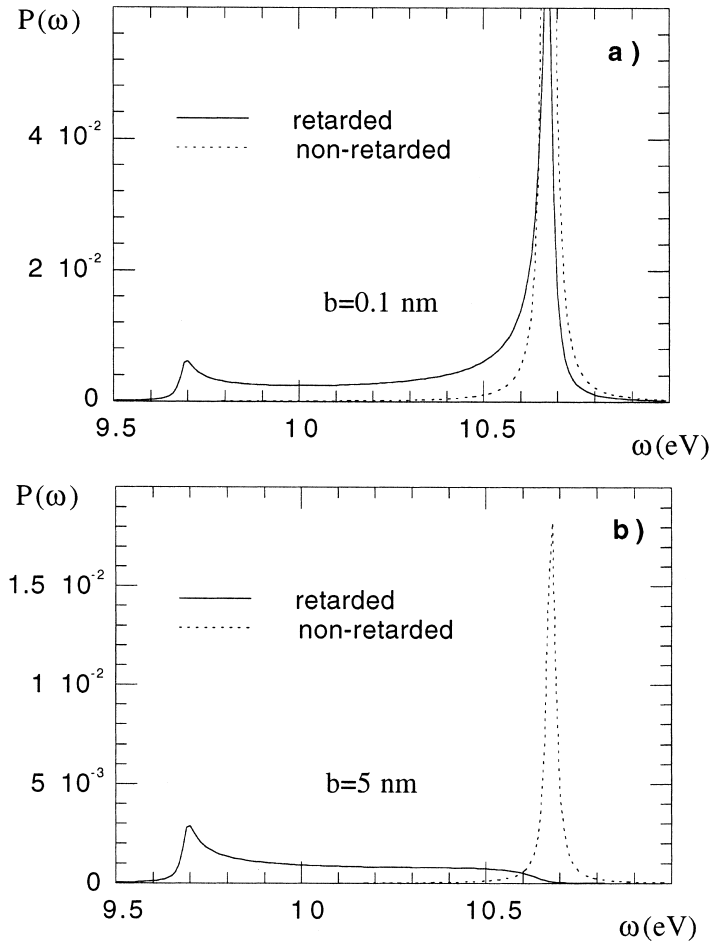


Fig. 3. Retarded (solid line) and non-retarded (dashed line) energy loss probability per unit length for electron moving parallel to metallic surface ( $\omega_p = 15.1$  eV,  $\gamma = 0.027$  eV). Corresponding impact parameters are: (a)  $b = 0.1$  nm; and (b)  $b = 5$  nm. Beam energy is 100 keV ( $v \sim 0.55c$ ).

allow plasmons to decay into photons [52]. The larger the retardation time  $b/c$  is, the larger this effect becomes.

In insulators, besides the retardation effect, *Cherenkov emission* becomes possible. In Fig. 4, we plot the spectra corresponding to an  $\text{Al}_2\text{O}_3$  surface, for two different impact parameters. In both plots, there are energy losses in the region of the gap (0–7 eV), which are due to the Cherenkov emission. Such losses are not present in the spectra corresponding to a 100 keV beam, because then the velocity is below the threshold of the Cherenkov radiation [ $\epsilon(\omega) \sim 3$  in this region]. This effect is relatively more strong as  $b$  becomes large, because it comes from the contribution of the term  $\sqrt{1 - \epsilon\beta^2}$  to the imaginary part of  $\mu$  in (2.27), so it is only relevant for small values of  $q_y$ . This observation indicates that, for non-penetrating trajectories of the probe, Cherenkov emission is relevant only in large targets.

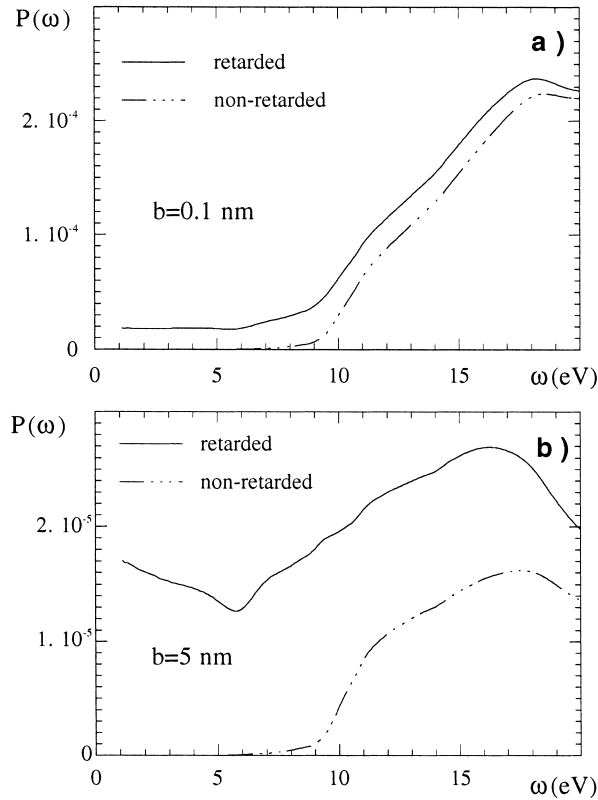


Fig. 4. Retarded (solid line) and non-retarded (dashed line) energy loss probability per unit length for electron moving parallel to  $\text{Al}_2\text{O}_3$  surface. Corresponding impact parameters are: (a)  $b = 0.1$  nm; and (b)  $b = 5$  nm. Beam energy is 200 keV ( $v \sim 0.70c$ ). Experimental dielectric functions have been used [106].

For large impact parameters, the retarded expression leads to a significantly better agreement with experimental intensity of surface loss peaks than the non-retarded one [31]. The importance of taking into account the relativistic corrections, to interpret with full particulars the experimental spectra, has been emphasised by Moreau et al. [54].

In addition to the planar geometry, relativistic corrections have been evaluated for other simple geometries such as spheres [55,56] and cylindrical cavities [57,58]. Recently, García de Abajo and Howie [59] have developed a numerical procedure, which allows the calculation of the retarded energy loss probability, in targets of general geometry.

As a finishing remark, we notice that we have used the force as a magnitude to represent the interaction. Nevertheless, many problems involving the charge–surface interaction are usually tackled through a Hamiltonian approach, where the interaction is derived from the static potential energy. The potential energy  $V(z)$  is then the electrostatic energy stored by the probe–surface system, when the probe is at a distance  $z$  from the surface, and is given by [18]:

$$V(z) = \frac{1}{2} Z \phi_{\text{ind}}(\omega = 0, \mathbf{r}) |_{\text{traj}} = -\zeta(\omega = 0) \frac{Z^2}{4z}, \quad (2.30)$$

where we have used (2.8). Note that although  $V(z)$  differs by a factor  $\frac{1}{2}$  from the product  $Z\phi_{\text{ind}}$ , this expression leads to the right asymptotic value of the force, as given by (2.22).

### 3. Excitation of electronic states by extended beam

The understanding and interpretation of energy filtered images in STEM poses the basic problem of spatial resolution, i.e., the distance at which the probe can significantly produce on given excitation.

From a theoretical point of view, neglecting the technical limitations of the instruments, there are three lengths relevant to this analysis: the spatial extension of the excited states of the target; the range of the Coulomb potential; and, finally, the beam spatial spread. Now, we concentrate on this last parameter, although in current microscopes the width is as small as 0.2 nm, a length which poses an obvious limit to the resolution, it raises the question of what is the error made when one considers the beam as a fast classical electron moving with a fixed impact parameter, neglecting the wave nature of the beam electrons.

Following [60], we consider the excitations of core electrons by a broad coherent electron beam. The electronic states of the target are represented by a complete set of eigenstates  $|n\rangle$  of energy  $\omega_n$ , while the beam is described by a plane wave  $\Omega^{-1/2} e^{i\mathbf{p}\cdot\mathbf{r}}$ , where  $\Omega$  is the normalisation volume. In the framework of the time-dependent perturbation theory, the cross-section  $\sigma_{n0}$  for the transition from the target ground state  $|0\rangle$  to a final excited state  $|n\rangle$  is given by:

$$\sigma_{n0} = \frac{4}{v\Omega} \int \frac{d\mathbf{q}}{q^4} |\rho_{n0}|^2 \delta \left[ \mathbf{v}\mathbf{q} - \frac{q^2}{2} - \omega_{n0} \right], \quad (3.1)$$

where  $\omega_{n0} = \omega_0 - \omega_n$  is the energy of the transition,  $\mathbf{v} = \mathbf{p}$  is the velocity or initial momentum of the electrons of the beam and  $\mathbf{q}$  is the momentum transfer. The matrix elements of the density operator are given by:

$$\rho_{n0} = \langle n | \sum e^{i\mathbf{q}\mathbf{r}} | 0 \rangle, \quad (3.2)$$

where the sum extends to all the atoms of the target. In (3.1), the delta function arises from energy conservation, and the term  $\frac{1}{2}q^2$  is the incident electron recoil. For STEM electrons and small scattering angles, this term is very small in comparison to  $\mathbf{v}\mathbf{q}$  and can be neglected. Then, one can write (3.1) as follows:

$$\sigma_{n0} = \int d\mathbf{b} |a_{n0}(\mathbf{b})|^2, \quad (3.3)$$

where  $\mathbf{b}$  is the spatial variable conjugate to the component of the momentum transfer and  $a_{n0}(\mathbf{b})$  is given by:

$$a_{n0}(\mathbf{b}) = \frac{1}{i} \int_{-\infty}^{\infty} dt e^{i\omega_{n0}t} \left\langle n \left| \sum \frac{1}{|\mathbf{b} + \mathbf{v}t - \mathbf{r}|} \right| 0 \right\rangle, \quad (3.4)$$

which can be regarded as the probability amplitude that the system experiences a transition  $|0\rangle \rightarrow |n\rangle$ , due to the interaction with an electron moving in a classical trajectory at impact parameter  $\mathbf{b}$ . Eq. (3.3) states that the probability of inducing an atomic transition by a broad beam can be evaluated as the incoherent sum of probabilities for different impact parameters. All the quantal effects arise from the recoil term in (3.1), which has been calculated by Ritchie and found to be negligible for STEM electrons [60]. As Ritchie stated, the higher the velocity of the incident electron, the more classical is its behaviour with respect to energy transfer to matter.

The impact parameter dependence of the probability amplitude can be better studied by writing (3.4) as:

$$a_{n0}(\mathbf{b}) = -\frac{2i}{v} \left\langle n \left| \sum e^{i\frac{W_{n0}x}{v}} K_0 \left[ \sqrt{(b_y - y)^2 + (b_z - z)^2} \frac{\omega_{n0}}{v} \right] \right| 0 \right\rangle, \quad (3.5)$$

where we have assumed that the beam is oriented in the direction of the  $x$ -axis. The operator in the matrix element of (3.5) is basically the  $\omega$ -component of the Coulomb potential created by the particle, and falls off outside a region of size  $v\omega_{n0}^{-1}$  around the microprobe ( $\sim 1$  nm for 100 keV electrons and 100 eV excitations). Nevertheless, due to the orthogonality of the wave functions, the matrix element in (3.5) takes relevant values only when the operator varies very quickly in the region where the overlap of the wave functions occurs. Taking into account the behaviour of the Bessel function, one concludes that the impact parameter relative to the atom should be smaller than the spatial extension of the

electronic states. Consequently, these inelastic processes effectively take place, when the beam impinges directly on the atom. Since these excitation energies do not depend on the target shape, this technique has been commonly used to identify single atoms in thin crystals [61] and to establish chemical information of selected parts of the sample [9,62].

Ritchie and Howie have generalised the analysis for collective excitations of the target [63]. Let us suppose a microprobe moving along the  $x$ -axis, centred at a position given by  $\mathbf{b}$  in the  $yz$ -plane. Its wave function can be represented as:

$$\psi(\mathbf{r}) = \frac{1}{\sqrt{\Omega}} \Delta(\mathbf{r}_{\perp} - \mathbf{b}) e^{ik_0 x}, \quad (3.6)$$

where  $\mathbf{r}_{\perp}$  stands for the projection of  $\mathbf{r}$  in the  $yz$ -plane. The function  $|\Delta(\mathbf{r}_{\perp} - \mathbf{b})|^2$  describes the transverse shape of the wave packet. To calculate the probability of exciting plasmons of energy  $\omega$ , when the beam crosses near a target, we proceed as above. Again, the electron recoil is neglected and we assume that all the inelastically scattered electrons are collected, then the probability of losing energy  $\omega$  can be written as:

$$P(\omega) = \int d\mathbf{r}_{\perp} |\Delta(\mathbf{r}_{\perp} - \mathbf{b})|^2 P_{\text{class}}(\omega, \mathbf{r}_{\perp}), \quad (3.7)$$

where  $P_{\text{class}}(\omega, \mathbf{b})$  stands for the energy loss probability corresponding to a classical electron moving at the impact parameter  $\mathbf{b}$ . Eq. (3.7) states that in valence EELS the beam can be considered as an incoherent sum of classical electrons. The condition of collecting all the electrons implies that the momentum transfer must be small enough, so that all the electrons emerge with a scattering angle smaller than the spectrometer aperture. In the usual experimental set up, the spectrometer aperture is  $\vartheta_m \sim 8.10^{-3}$  rad, a value large enough, so that the condition of collecting most of the scattered electrons is reasonably fulfilled.

Batson [64] discussed the effect of the real limited spectrometer aperture as an effective cut-off to the momentum transfer,  $q_{\text{max}}$ , which imposes on the spatial resolution a limit of about  $q_{\text{max}}^{-1} \sim \{v\vartheta_m\}^{-1}$ , a length of the order of 0.1 nm. The author concluded that, in real STEM situations, this classical approach provides a good description of the inelastic scattering.

#### 4. Spatial resolution in valence EELS

Valence loss spectroscopy benefits from the relative high intensity, which allows energy selected images to be obtained without strong damage of the sample. Experimental observations by Batson [2,3], Wang and Cowley [65,168–170], Walsh [57], Howie and Walsh [66] and Ugarte et al. [5] have shown the ability of this technique to reveal surface or bulk structures of microsamples. Nevertheless, the interpretation of the loss spectra and filtered images is much more complicated. First of all, the energy of these excitations depends, not only on the composition

of the sample region under study, but also strongly on the surface shape, on the neighbouring media and on the coupling with other parts of the sample. In addition, the collective excitations of the valence electrons (plasmons) are not spatially localised, so one cannot expect the same high resolution obtained for core electron excitations.

Let us study the energy deposited by a fast electron in a small volume  $dV$  of the sample. We assume that the electron is moving with constant velocity  $v$  and impact parameter  $b$  far away from the sample, so we can assume that the electric field created by the probe is at each time uniform around the sample. Then the energy loss rate in this volume is given by:

$$\frac{dW(t)}{dV} = \mathbf{E}(t) \frac{\mathbf{P}(t)}{dt}, \quad (4.1)$$

where  $\mathbf{E}$  and  $\mathbf{P}$  are the electric field and the polarisation, respectively. Neglecting the momentum dependence of the dielectric response function, one gets  $\mathbf{E}(\omega) = \zeta(\omega)\mathbf{P}(\omega)$ , where  $\zeta(\omega)$  is a response function, which depends on the dielectric nature and shape of the whole sample. The total energy loss deposited in this volume is obtained by integrating (4.1) along the trajectory. Then, the energy loss density can be easily written in terms of the  $\omega$ -component of the electric field:

$$\frac{dE_{\text{loss}}}{dV} = \frac{1}{\pi} \int_0^{\infty} \omega d\omega \text{Im}\{\zeta(\omega)\} |\mathbf{E}(\omega)|^2, \quad (4.2)$$

which can be interpreted in terms of the probability  $P(\omega)$  of producing inelastic excitations of energy  $\omega$ . Neglecting the relativistic corrections, the electric field can be obtained from (B7):

$$|\mathbf{E}(\omega)|^2 = \frac{4\omega^2}{\pi v^4} \left\{ K_0^2 \left[ \frac{\omega b}{v} \right] + K_1^2 \left[ \frac{\omega b}{v} \right] \right\}, \quad (4.3)$$

where  $K_{0,1}$  are the modified Bessel functions. For large values of  $b$ , one can use the asymptotic expansion of these functions and the loss probability per unit volume,

$$\frac{dP(\omega)}{dV} = \frac{4}{\pi^2 v^2} \text{Im}\{\zeta(\omega)\} \left[ \frac{\omega}{v} \right]^2 \left\{ K_0^2 \left[ \frac{\omega b}{v} \right] + K_1^2 \left[ \frac{\omega b}{v} \right] \right\} \quad (4.4)$$

behaves as  $\exp[-(2\omega b/v)]$ . Eq. (4.4) features the impact parameter dependence of the energy loss probability ruled by the scale factor  $\sim v\omega^{-1}$ . For a 10 eV loss and a beam energy of 100 keV, this leads to a distance of about 10 nm. This length determines the size of the target region around the trajectory, in which the probe can excite efficiently inelastic processes of energy  $\omega$ , so it provides the spatial resolution in valence EELS experiments, as discussed in connection with Fig. 1(b).

This result can be obtained in a simple way by means of a simple flight time argument [18]: the duration of the electric pulse  $\tau$  created by the probe is  $\tau \sim bv^{-1}$ , which leads to the cut-off impact parameters  $b_c \sim v\omega^{-1}$ .

Such an exponential dependence, derived from (4.4), has been found in many experiments with different surface shapes, as shown in Fig. 5.

Note that this argument is valid for surface excitations: bulk plasmons can be excited only when the probe moves through — or very near to — the medium. This approach is valid when the probe moves far away from the target, so the response function  $\zeta(\omega)$  has no bulk contribution. This fact can be seen in energy-selected images [2,5]; in general, the images corresponding to bulk losses are clear and the shape of the sample is sharply defined, while those corresponding to surface losses are much more diffuse. In the last case, the size of the illuminated area does not provide straight information about the thickness or size of the specimen, but is given basically by the length  $v\omega^{-1}$ .

On the other hand, the coupling between different parts of the specimen also occurs through the Coulomb potential, therefore, this coupling will be ruled by the same typical interaction length. This length imposes, at any beam position, a limit to the size of the region around the sample, which is effectively coupled to it and is, therefore, relevant to understanding the loss spectra. This means that targets, which locally do not differ significantly in a range of about  $v\omega^{-1}$ , will lead to similar loss spectra. As a consequence, in targets with smooth surfaces (spheres,

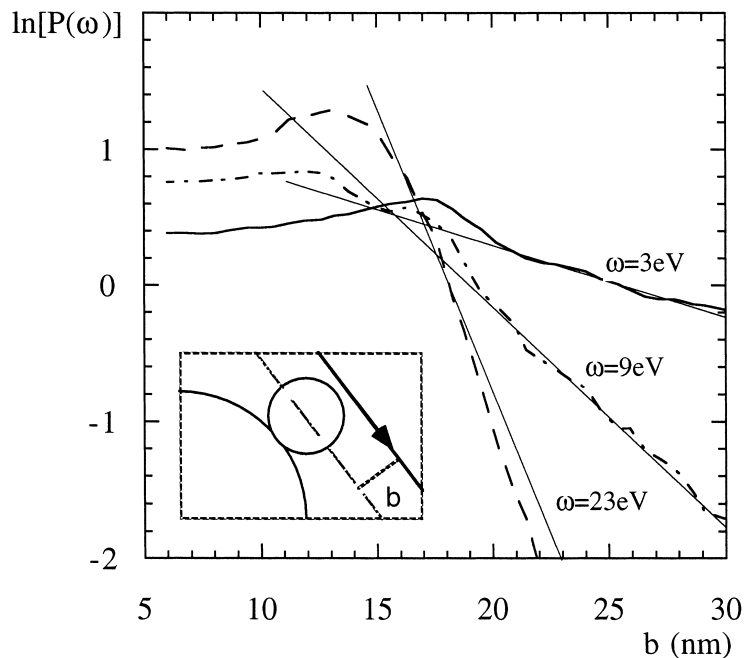


Fig. 5. Excitation probabilities for three different surface modes of system of two interpenetrating Si spheres. Experimental data have been taken from [5]. Continuous lines show asymptotic behaviour derived from (4.4). Pre-exponential factors in theoretical plots have been chosen to fit experimental curves.

cylinders, etc.), the planar spectrum is always recovered in the limit of a small curvature.

As we have pointed out before, retardation effects can be relevant at large impact parameters. Nevertheless, as shown in experiments (see for instance Fig. 5), it provides just a correction to the asymptotic exponential decay.

## 5. Theoretical approaches to surface–probe interaction

Although many quantal models have been developed to describe the interaction of fast electrons with matter, most of them used simple theoretical approaches to the excitation of the target. Here, we present a quantal model which allows the use of any dielectric function. Such a general formulation of the problem of the interaction of a quantal probe with a dielectric target can be used with any dielectric function, leading to an expression suitable for EELS in electron microscopy. This expression can be recovered by considering the electron as a classical particle. The equivalence between both descriptions confirms the suitability of (3.7).

### 5.1. Quantal model: self-energy formalism

The interaction between an external charged particle and a polarisable medium is described in the quantal description through a complex function  $\Sigma = \Sigma_{\text{R}} - i\Sigma_{\text{I}}$  called *self-energy* [67–69]. A detailed description of the formulation and different points of views and approaches can be found in Refs. [70,71]. Here, we apply the self-energy formulation to the problem of the energy loss in STEM [72,73].

In the self-energy treatment of scattering experiments, the probe is represented by a wave function that polarises the target, which reacts back on the probe changing its quantum state. The real part of the self-energy  $\Sigma_{\text{R}}$  is the image potential, giving the energy shift  $\Delta E$  of the incoming particle, due to virtual excitations of the medium. The imaginary part  $\Sigma_{\text{I}}$  is directly related to the energy loss, experienced by the probe charge, due to real excitations produced in the target.

Let us consider the electron probe in an initial state  $\Phi_0$  with energy  $E_0$ . The mean energy of the incoming electron, due to the non-local interaction with the medium, is written as the average of an *effective potential operator*  $V_{\text{eff}}(\mathbf{r})$

$$\Sigma_0 = \int d\mathbf{r} \Phi_0^*(\mathbf{r}) V_{\text{eff}}(\mathbf{r}) \Phi_0(\mathbf{r}), \quad (5.1)$$

which, in fact, can be expressed in terms of the non-local self-energy as:

$$V_{\text{eff}}(\mathbf{r}) \Phi_0(\mathbf{r}) = \int d\mathbf{r}' \Sigma(\mathbf{r}, \mathbf{r}', E_0) \Phi_0(\mathbf{r}'). \quad (5.2)$$

The self-energy can be written within the pair approximation [67,74] in terms of

the *Green's function* (GF)  $G(\mathbf{r}, \mathbf{r}', \omega + E_0)$  and the causal screened interaction  $W(\mathbf{r}, \mathbf{r}', \omega)$ ,

$$\Sigma(\mathbf{r}, \mathbf{r}', E_0) = \frac{i}{2\pi} \int d\omega W(\mathbf{r}, \mathbf{r}', \omega) G(\mathbf{r}, \mathbf{r}', \omega + E_0) e^{i\delta\omega}. \quad (5.3)$$

$\delta$  being a positive infinitesimal quantity, indicating that the integration in  $\omega$  must be taken in the upper sub-plane,  $\text{Im}(\omega) > 0$ . The causal screened interaction is the same function defined in Appendix B. The GF can be written as the following summation over a complete set of the final states  $\Phi_f(\mathbf{r})$  with energy  $E_f$ :

$$G(\mathbf{r}, \mathbf{r}', \omega + E_0) = \sum_f \frac{\Phi_f^*(\mathbf{r}') \Phi_f(\mathbf{r})}{\omega + E_0 - E_f}. \quad (5.4)$$

Then, by replacing (5.2)–(5.4) in (5.1), we have:

$$\Sigma_0 = \frac{1}{\pi} \sum_f \int d\omega \, d\mathbf{r} \, d\mathbf{r}' \frac{\Phi_f^*(\mathbf{r}') \Phi_0(\mathbf{r}') \Phi_f(\mathbf{r}) \Phi_0^*(\mathbf{r})}{\omega + \Delta E + i\delta} \text{Im}\{W(\mathbf{r}, \mathbf{r}', \omega)\}, \quad (5.5)$$

where  $\Delta E = E_f - E_0$ .

Eq. (5.5) is of general validity; in addition to EELS in STEM, it has been used in other problems involving probes and surfaces, such as image states [75].

As we have already pointed out, the real part of the self-energy  $\Sigma_R$  is related to the dynamic image potential and can be interpreted as the energy needed for the probe to approach the target ([18]). To deal with the energy losses in inelastic scattering processes, the calculation of the imaginary part of the self-energy  $\Sigma_I$  is of special interest, since it is related to the energy-loss rate  $\gamma$  experienced by the incoming particle. The effect of inelastic scattering can be represented by introducing an *imaginary optical potential* in the one-particle Schrödinger equation [76], which leads to a time-dependence in the probability of the incident particle as  $e^{2\Sigma_I t}$ , from where we can define the imaginary part of the self-energy,

$$-\Sigma_I = \frac{1}{2\tau} = \frac{\Gamma}{2}, \quad (5.6)$$

where  $\tau$  is a mean inelastic collision time, the lifetime of a coherent fast particle wave function, and  $\Gamma$  is the energy width of the level.

Descriptions of energy loss experiments are performed mostly in terms of the probability per unit length  $P(\omega)$  of losing energy  $\omega$  or the inverse mean free path  $\Lambda^{-1}$ , magnitudes that are both related to the imaginary part of the self-energy. For a probe moving with velocity  $v$ , these relations are

$$-\Sigma_I = \frac{v\Lambda^{-1}}{2} = \frac{v}{2} \int_0^\infty d\omega P(\omega). \quad (5.7)$$

Expressions (5.5) and (5.7) have been used to study the energy loss experienced by a broad beam, when interacting with spherical and cylindrical targets [72,77]. For

a spherical target, the classical expression obtained by Penn and Apell [78] is recovered.

The above formalism can be applied to the case of well-focused STEM beams. In this case, the incoming electron wave function is approximated as in (3.6), where  $|\Delta(\mathbf{r}_\perp - \mathbf{b})|^2 \sim \delta(\mathbf{r}_\perp - \mathbf{b})$ . Then, neglecting the recoil term in  $\Delta E$  and transforming the summation over final states into an integral over momentum transfer, we finally obtain the following expression for the energy loss probability [73]:

$$P(\omega) = \frac{1}{\pi v^2} \int_{-\infty}^{\infty} dx' \int_{-\infty}^{\infty} dx \operatorname{Im}\{W(\mathbf{r}, \mathbf{r}', \omega) e^{i\frac{\omega x}{v}(x-x')}\} |_{\text{traj}}, \quad (5.8)$$

where both  $\mathbf{r}$  and  $\mathbf{r}'$  are evaluated along the trajectory. Eq. (5.8) accounts for the total energy loss probability, containing bulk and surface contributions.

The main advantage of this method, in relation to other quantal methods, is that it allows the use of any dielectric function. In addition, (5.8) is easily computable, since it only involves a double integral. The connection between this quantal formalism and the classical approaches is presented in the next section.

## 5.2. Classical approach

Expression (5.8), although obtained in a quantal context, can also be derived from a classical point of view. In the classical framework, the interaction is given by the induced potential, which in turn can be expressed in terms of the screened interaction and the charge density (see Appendix B). The charge density is given by (2.2). So, the induced potential is given by:

$$\phi(\mathbf{r}, t) = -\frac{1}{2\pi v} \int_{-\infty}^{\infty} d\omega \int_{-\infty}^{\infty} dx' e^{i\frac{\omega x}{v}(x'-vt)} W(\mathbf{r}, \mathbf{r}', \omega) |_{\text{traj}}. \quad (5.9)$$

The total energy loss  $\Delta E$  can be calculated as the work developed against the electric field acting on the electron along the whole trajectory:

$$\Delta E = \int_{-\infty}^{\infty} \left. \frac{\partial \Phi}{\partial x} \right|_{\text{traj}} dx = \int_{-\infty}^{\infty} d\Phi |_{\text{traj}} - \int_{-\infty}^{\infty} \left. \frac{\partial \Phi}{\partial t} \right|_{\text{traj}} dt. \quad (5.10)$$

In most cases of interest, the potential is the same at both ends of the trajectory, i.e.,  $\Phi(x = -\infty) = \Phi(x = \infty)$ , therefore, the integration in  $\Phi$  on the right-hand-side of (5.10) vanishes, whence,

$$\Delta E = -\frac{1}{v} \int_{-\infty}^{\infty} \left. \frac{\partial \Phi}{\partial t} \right|_{\text{traj}} dx. \quad (5.11)$$

By taking into account that  $W(\mathbf{r}, \mathbf{r}', -\omega) = W^*(\mathbf{r}, \mathbf{r}', \omega)$ , one can write (5.11) as an integral over the positive values of  $\omega$  and (5.8) is straightforwardly recovered.

In the classical formalism, the condition that  $W(\mathbf{r}, \mathbf{r}', \omega)$  is evaluated along the

trajectory can be explicitly incorporated by writing it in terms of the charge density, so that the probability is written as:

$$P(\omega) = \frac{1}{\pi} \int_{-\infty}^{\infty} d\mathbf{r}' \int_{-\infty}^{\infty} d\mathbf{r} \operatorname{Im}\{\rho^*(\mathbf{r}, \omega) W(\mathbf{r}, \mathbf{r}', \omega) \rho(\mathbf{r}', \omega)\}. \quad (5.12)$$

In this way, the energy loss probability can be understood as the average value of the imaginary part of the screened interaction over the whole trajectory.

Furthermore, (5.12) has a wider range of applicability, it is not just restricted to the special trajectory considered in our problem, as was the case in (5.8). Note that the validity of both (5.8) and (5.12) is restricted to those situations, when the previously mentioned condition on the potential is applicable. That condition can be better understood within the framework of the time-dependent perturbation theory [79]. Thus, one avoids the elastic contributions to the energy loss, which vanish when considering the whole trajectory. Such a condition is trivially fulfilled in the cases of finite targets, reflection at planar surfaces or an electron crossing a film or cylinder, since the potential then vanishes at both extremes of the trajectory.

These expressions allow us to calculate the energy loss, due to the whole trajectory (which is just the magnitude measured in the EELS analyser), and do not give the stopping power at different trajectory points. Nevertheless, in the case of an electron moving parallel to an interface, which exhibits translational invariance in the probe direction (planes, cylinders, films, etc.), the former condition is fulfilled at any point of the trajectory, so one can obtain in the same way the expression for the energy loss probability per unit length:

$$\frac{P(\omega)}{dx} = \frac{1}{\pi v^2} \int_{-\infty}^{\infty} dx \operatorname{Im}\{W_{\text{ind}}(\mathbf{r}, \mathbf{r}', \omega) |_{\text{traj}} e^{i\omega x/v}\}. \quad (5.13)$$

The fact that (5.12) can be obtained from both quantal and classical descriptions of the beam is a strong corroboration of Ritchie and Howie's statement given by (3.7), in an extreme case, where all the values of the transverse momentum are present in the quantal wave function.

Recently, Cohen et al. [80] have studied the quantal effects derived from the spatial extension of the beam. They write the wave function as in (3.6) and then expand the lateral function  $\Delta$  in the basis of eigenfunctions of a box. Their results do not basically contradict those of the classical theory, though Echenique et al. [81] have criticised the suitability of their basis to describe the final states.

## 6. EELS in planar surfaces

The planar surface provides a simple geometric model to study the basic features of the interaction between the probe and a surface, as mentioned in Section 2. Here, we study this basic geometry, in order to understand many different aspects of interest. First, we study EELS of an electron interacting with a

thin film, which allows the study of two relevant problems: the sensitivity of the EELS technique to sub-surface structures, and the energy loss experienced when the probe penetrates the specimen. Finally, the reflection on a planar surface is studied.

### 6.1. Sub-surface sensitivity

To study the first problem, we consider a sample formed by a semi-infinite medium characterised by its dielectric function  $\epsilon_2(\omega)$ , covered by a layer of dielectric function  $\epsilon_1(\omega)$  and thickness  $a$ . We assume that the outer medium is a vacuum. In a situation where the electron is moving outside and parallel to the surfaces at impact parameter  $b$  (see inset in Fig. 6), one may wonder about the ability of the EELS technique to detect the inner medium, and how it appears in the loss spectrum.

Takimoto [17] investigated the energy loss experienced by a fast electron moving parallel to a metallic film. For the more general case, the screened interaction can be easily calculated by Fourier-transforming (B2) in the surface plane (we take the  $z$ -axis in the direction normal to the surface, with the origin on the external interface):

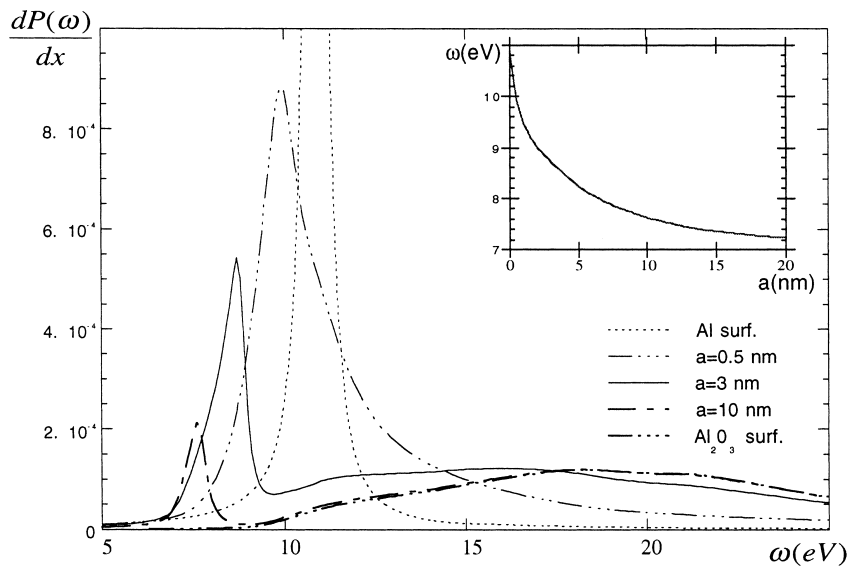


Fig. 6. Energy loss spectra corresponding to clean Al surface (dotted line) and Al surface coated with  $\text{Al}_2\text{O}_3$  layer, for different values of oxide thickness. Impact parameter relative to outer surface of layer has been kept to 1 nm. Dependence of surface plasmon peak with oxide thickness is shown in inset figure. Experimental data of dielectric functions have been used [105].

$$W(\mathbf{r}_\perp, \mathbf{r}'_\perp, z, z', \omega) = \frac{1}{(2\pi)^2} \int d^2\mathbf{q} e^{i\mathbf{q}(\mathbf{r}_\perp - \mathbf{r}'_\perp)} W(\mathbf{q}, z, z', \omega), \quad (6.1)$$

where the vector  $\mathbf{q}$  is the projection of the momentum in the  $xy$ -plane and  $\mathbf{r} = (\mathbf{r}_\perp, z)$ . For the case when both  $\mathbf{r}$  and  $\mathbf{r}'$  are in the outer medium, the induced screened function is given by:

$$W(\mathbf{q}, z, z', \omega) = \frac{2\pi}{q} e^{-q(z+z')} \frac{\xi_{21} + \xi_{10} e^{2qa}}{\xi_{21}\xi_{10} + e^{2qa}}, \quad (6.2)$$

where  $q$  stands for  $|\mathbf{q}|$  and  $a$  is the layer thickness. The  $\xi$ -functions are the planar response functions of both interfaces; i.e.:

$$\xi_{10} = \frac{\epsilon_1 - 1}{\epsilon_1 + 1}, \quad \xi_{21} = \frac{\epsilon_2 - \epsilon_1}{\epsilon_2 + \epsilon_1}. \quad (6.3)$$

From (5.13) one can obtain, in a straightforward way, the energy loss probability per unit length:

$$\frac{dP(\omega)}{dx} = \frac{2}{\pi v^2} \int_1^\infty \frac{dt}{\sqrt{t^2 - 1}} e^{\frac{-2\omega b}{v} t} \text{Im} \left\{ \frac{\xi_{21} + \xi_{10} e^{\frac{2\omega a}{v} t}}{\xi_{21}\xi_{10} + e^{\frac{2\omega a}{v} t}} \right\}, \quad (6.4)$$

where  $b$  is the impact parameter (relative to the external surface).

Not that, in the limit of large thickness,  $a \gg v\omega^{-1}$ , the function to be integrated in (6.4) becomes the integral representation of the Bessel function  $K_0$ , thus, one recovers (2.11) corresponding to a semi-infinite medium of dielectric response  $\epsilon_1$ . On the other hand, the limit of a semi-infinite medium of dielectric response  $\epsilon_2$  could be formally recovered, when  $a$  is strictly zero; nevertheless, even for very small values of  $a$  ( $a \ll v\omega^{-1}$ ), the coupling between both surfaces, given by the term  $e^{2\omega a/v}$  in (6.4), is strong enough so that the loss spectrum differs very much from that corresponding to the clean surface. Eq. (6.4) states that EELS is sensitive to large sub-surface structures up to a depth of the order of  $v\omega^{-1}$ .

In Fig. 6, we illustrate this point by plotting the loss spectra obtained from (6.4) corresponding to an Al surface, covered by an  $\text{Al}_2\text{O}_3$  layer, for different values of the layer thickness. The main feature is the dramatic change in the Al surface peak at 10.7 eV, which suffers a red shift, even for a thin covering of oxide, as shown in the inset. Note that the sensitivity of EELS is not uniform over all the spectrum range; in the region of the  $\text{Al}_2\text{O}_3$  broad surface peak, there is no trace of the Al medium, even for a 3 nm thick layer, while the sharp loss peak, which is due to the coupling between both surfaces, can be detected at much thicker covering. The different sensitivity derives from the range of the  $\omega$ -component of the Coulomb potential: the smaller the excitation energy, the deeper the EELS detection ability. The behaviour shown is in agreement with experiments performed by Batson [4], who also observed it on Al particles, where a very thin oxide layer provoked large changes in the loss peaks [2].

## 6.2. EELS in thin films

The inelastic interaction between a normally incident-fast electron and a film was first studied by Ritchie [8], using the *Bloch hydrodynamic model*. The energy loss probability  $P(\omega)$  was written as a sum of the contributions of excitations of different momentum transfer  $q$ :  $P(\omega) = \int_0^\infty 2\pi q dq P(q, \omega)$ , where the surface contribution to the excitation probability  $P(q, \omega)$  is given by:

$$P_{\text{surf}}(q, \omega) = \frac{1}{\pi^2 v^2} \frac{2q}{\left\{q^2 + \frac{\omega^2}{v^2}\right\}^2} \text{Im} \left\{ \frac{1 - \epsilon}{\epsilon} \frac{2(\epsilon - 1) \cos \frac{\omega a}{v} + (\epsilon - 1)^2 e^{-qa} + (1 - \epsilon^2) e^{qa}}{(\epsilon - 1)^2 e^{-qa} - (\epsilon + 1)^2 e^{qa}} \right\}. \quad (6.5)$$

In addition to the surface contribution, one has to consider the bulk losses corresponding to a path of length  $a$  inside the medium. For a film characterised by a Drude function, the energies of the excitations are determined by the zeros of the denominator, i.e., solutions of the equations  $\epsilon = 0$  and  $(\epsilon - 1)^2 e^{-qa} - (\epsilon + 1)^2 e^{qa} = 0$ , which correspond to the excitation of bulk and surface plasmons, respectively. For a metal, the energy of the surface plasmons  $\omega_\pm$  is given by the dispersion relation:

$$\omega_\pm = \omega_p \sqrt{\frac{1 \pm e^{-2qa}}{2}}. \quad (6.6)$$

The splitting of the surface modes is due to the coupling between both interfaces. The low mode,  $\omega_-$ , corresponds to a symmetric distribution of charge density at both faces of the film [82]. The energy of this symmetric mode is lowered with respect to  $\omega_s$ , because of the screening [ $\epsilon(\omega)$  is negative in this frequency range]. The high mode,  $\omega_+$ , corresponds to the antisymmetric charge distribution. For a given thickness, the probability of exciting one of these modes depends on whether the probe finds both surface charge densities in phase or not, i.e., it is basically ruled by the rate between the time spent to go across the film,  $av^{-1}$ , and the plasmon period  $2\pi\omega^{-1}$ . This rule can be visualised in Fig. 7, where we display the contribution of symmetric and antisymmetric modes to the total surface plasmon excitation probability. The maxima of the symmetric modes  $\omega_-$  are given by the quantisation relation:  $a\omega v^{-1} = 2\pi n$  ( $n$  integer), while that corresponding to  $\omega_-$  satisfies:  $a\omega v^{-1} = \pi n$  ( $n$  odd). The frequency involved in this expression is  $\omega_s$ , because, in the range of values of  $a$  where this condition is fulfilled  $a > v\omega_s^{-1}$ , the main contribution to the surface losses in (6.5) arises from  $q \sim \omega_s/v = a^{-1}$ , so the energy of the corresponding excitations, given by (6.6), are very close to  $\omega_s$ . For very thick films, both interfaces become uncoupled and the total probability tends to  $\pi v^{-1}$ ; then both modes have the same energy  $\omega_s$ , and the excitation of each

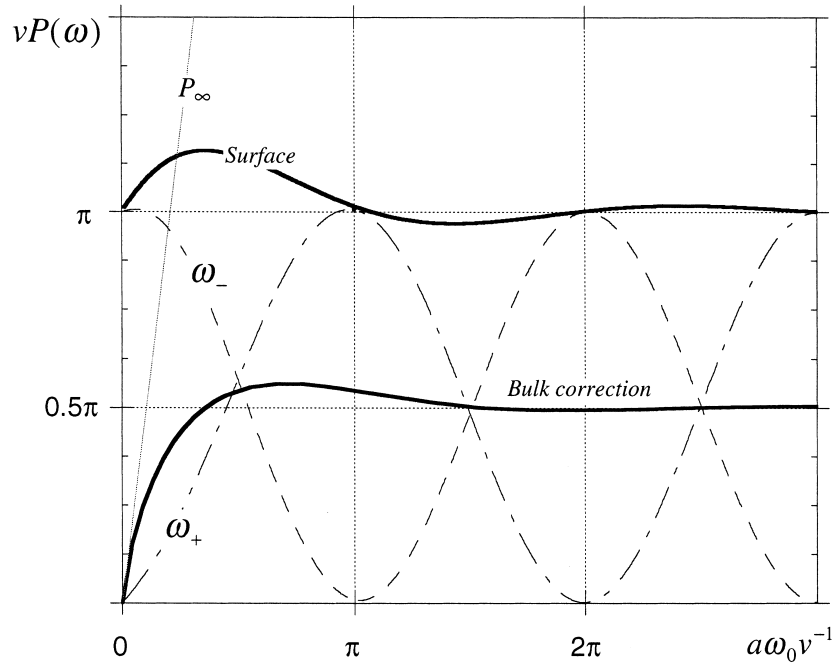


Fig. 7. Probability of exciting surface plasmons and surface bulk correction in film vs reduced thickness  $a\omega_0v^{-1}$ . In surface plots  $\omega_0$  is  $\omega_s$  and  $\omega_p$  in bulk correction. Drude dielectric function has been used. Sign of bulk corrections has been changed to fit it into plot. Loss probability corresponding to a path length in the bulk medium ( $P_\infty$ ) has also been plotted.

interface can be regarded as an independent process. For very thin films, although the energy loss probability also tends to the value  $\pi v^{-1}$ , the energy of the excited mode  $\omega_-$  tends to zero, hence, there is no energy loss.

In (6.5) the bulk contribution is a negative correction to the bulk losses, i.e., it determines the *begrenzung* effect found in Section 2 for trajectories inside the metal (2.16) and (2.17). In Fig. 7, the bulk correction has been plotted as a function of the film thickness. For a thickness larger than  $v\omega_p^{-1}$ , this term becomes constant,  $-(\pi/2v)$ . For very small values of the parameter  $t = a\omega_p v^{-1}$ , this term goes to zero as  $\sim(t/v) \ln(t)$ , i.e., slower than the direct bulk term, which is proportional to the film thickness  $t$ .

This work has been generalised to include arbitrary inclined trajectories and relativistic corrections [49,82].

### 6.3. Reflection in planar surface

A simple and useful model of inelastic scattering under glancing angle conditions and based on the classical dielectric excitation theory, has been used in

reflection high energy electron diffraction (RHEED) and reflection electron microscopy (REM) [30]. A detailed study of energy loss spectra under these conditions yields useful experimental information about the effective penetration depths [83,84]. For such trajectories, the probe experiences the inelastic interaction in a region very close to the surface, so the surface correction to the bulk peak is relevant to the calculation of the path length inside the medium. For a small enough incidence angle  $\vartheta$ , i.e., when the momentum transfer  $\sim v\vartheta \ll 1$ , the local dielectric approach is valid, and (5.12) can be used. In this case, the problem can be tackled by neglecting the deflection experienced by the probe near the surface and assuming that it reflects in the medium at a depth  $d$  from the surface, as shown in the inset of Fig. 8. The charge density can then be realistically described as:

$$\rho(\mathbf{r}, t) = \delta(x - v t \sin \vartheta) \delta(y) \{ \delta(z + v t \cos \vartheta) \Theta(-x) + \delta(z - v t \cos \vartheta) \Theta(x) \}, \quad (6.7)$$

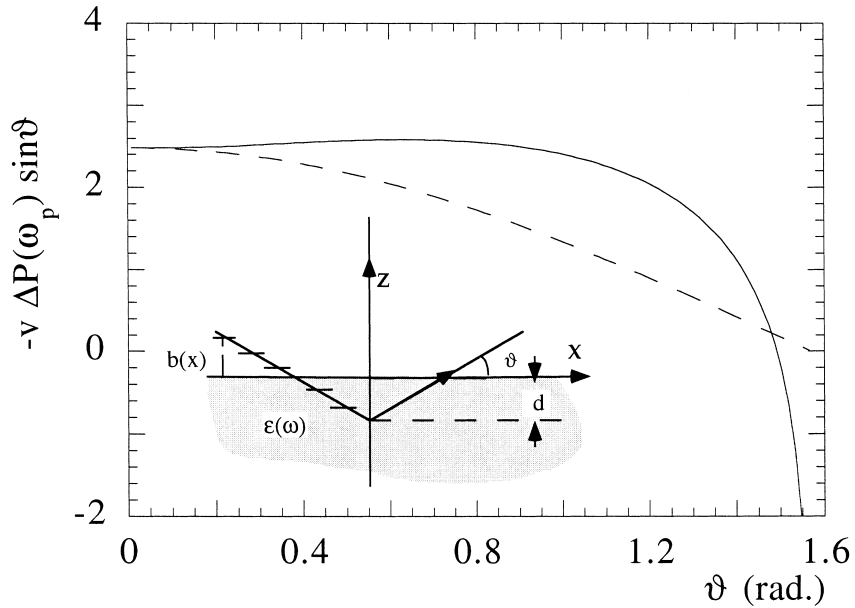


Fig. 8. Bulk correction to loss probability as a function of angle  $\vartheta$  for electron penetrating into metallic surface. Factor  $\sin \vartheta$  has been introduced to normalise plot to path length inside medium. Sign of this plot has been changed. Solid line corresponds to the results obtained through (6.8). Dotted line corresponds to Howie's parallel segment approximation. Penetration depth is  $d = 0.5v\omega_p^{-1}$ . Inset shows Howie's model.

where  $v$  is the velocity of the probe and  $\Theta(x)$  stands for the Heaviside function. In conjunction with (5.12), and using the planar screened function (B4), Eq. (6.7) straightforwardly results in the total loss probability. The surface contribution is given by:

$$\begin{aligned}
 P_{\text{surf}}(\omega) = & \frac{2}{\pi v \omega} \text{Im}\{\xi(\omega)\} \left\{ \left[ \int_0^{t_0} dt \int_0^{t_0} dt' + \int_{t_0}^{\infty} dt \int_{t_0}^{\infty} dt' \right] g(t, t', \vartheta) \right. \\
 & + 2 \int_0^{t_0} dt \int_{t_0}^{\infty} dt' f(t, t', \vartheta) \\
 & \left. - 2 \int_0^{t_0} dt Ci(t) \right\} - \frac{2}{\pi v \omega} \text{Im}\left\{ \frac{1}{\epsilon(\omega)} \right\} \left\{ \int_0^{t_0} dt \int_0^{t_0} dt' [g(t, t', \vartheta) - f(t, t', \vartheta)] \right. \\
 & \left. - 2 \int_0^{t_0} dt Ci(t) \right\},
 \end{aligned} \tag{6.8}$$

where  $\xi(\omega)$  is the planar surface response function,  $t_0 = \omega d \{v \sin \vartheta\}^{-1}$  is a dimensionless parameter and  $Ci(x)$  is the cosine integral function [19]. The functions  $f$  and  $g$  are given by:

$$\begin{aligned}
 g(t, t', \vartheta) = & \frac{\cos(t - t')}{\sqrt{(t - t')^2 \cos^2 \vartheta + (2t_0 - t - t')^2 \sin^2 \vartheta}} \\
 & + \frac{\cos(t + t')}{\sqrt{(t + t')^2 \cos^2 \vartheta + (2t_0 - t - t')^2 \sin^2 \vartheta}} \\
 f(t, t', \vartheta) = & \frac{\cos(t + t')}{\sqrt{(t + t')^2 \cos^2 \vartheta + (t - t')^2 \sin^2 \vartheta}}.
 \end{aligned} \tag{6.9}$$

Eq. (6.8) presents both surface and bulk terms. The first, containing the response function  $\xi(\omega)$ , describes the excitation of surface plasmons, while the second is the negative bulk correction (begrenzung) to be added to the bulk term corresponding to a path length,  $2d(\sin \vartheta)^{-1}$ , inside the medium.

In the case of non-penetrating trajectories  $d = 0$ ,  $t_0 = 0$ , the bulk correction vanishes and the surface excitation probability is given by:

$$P(\omega) = \text{Im}\{\xi(\omega)\} \frac{1}{v \omega \sin \vartheta}, \tag{6.10}$$

which for a metal leads to the known value  $P(\omega_s) = \pi(2v \sin \vartheta)^{-1}$  [85,86].

Fig. 8 shows the bulk correction versus the incidence angle  $\vartheta$  for a Drude metal.

Note that, for this dielectric function, the magnitude  $vP(\omega)$  only depends on the parameter  $t_0$ . Here, we see that for small values of  $\vartheta$  this correction goes as  $(\sin \theta)^{-1}$ , a law similar to that found for the surface excitations in the non-penetrating case. For  $\vartheta > 1$ , this correction increases and becomes positive. Nevertheless, in this region, the main contribution to the loss probability comes from the vertex of the trajectory, i.e., it strongly depends on the momentum transfer through the dielectric response, and results derived from a local approach are not reliable.

Howie proposed a method to tackle the problem of the interaction of a fast electron with a smooth surface by approaching the electron trajectories via a set of differential paths parallel to the surface, at instantaneous impact parameter  $b(x)$  (see inset in Fig. 8). The total loss probability is then obtained by integrating the component of the force normal to velocity, over the whole trajectory [87,88]. In Fig. 8, we see the results of this approach; for  $\vartheta < 0.2$ , both plots are almost identical, while for normal incidence, the surface contribution obtained through the simple model tends to zero, because of the projection used to calculate the force.

The agreement between both methods, for small values of  $\vartheta$ , confirms the applicability of the parallel segment approximation, which has been rigorously stated for electrons travelling at a grazing incidence near very large spheres [89] or cylinders [58]. It seems reasonable to think that this procedure is valid for studying the impact parameter dependence near any large interface, under grazing-incidence conditions.

## 7. EELS in small particles

Valence energy loss spectroscopy has been extensively used to study different structures of a nanometre scale. Fujimoto and coworkers [90,91] studied the energy loss of a broad beam interacting with a sphere of free electron gas.

Petersen [11] and Batson [92,2,3] proved the ability of this technique to reveal structural details in small particles, as well as the difficulty of interpreting the loss spectra. Further experimental works by Achèche et al. [93], Wang and Cowley [65,168–170], Howie and Walsh [66], Ugarte et al. [5] and Ouyang et al. [94] revealed the strong effects of the target shape, and coupling with other surrounding surfaces in the loss spectra. Here, we review the simplest model, that of an isolated sphere, and then study the coupling with the supporting surface and the effect of the shape of the particle. Next, we present a short discussion about retardation effects in these targets. Finally, we give an introduction to the problem of a target consisting of many small particles.

### 7.1. Isolated sphere

By applying the self-energy formalism, the energy loss probability corresponding to an electron interacting with an isolated sphere of dielectric function  $\epsilon(\omega)$  can be

easily obtained (see Appendix B):

$$P(\omega) = \frac{4a}{\pi v^2} \sum_{l=1}^{\infty} \sum_{m=0}^l \frac{2 - \delta_{m0}}{(l+m)!(l-m)!} \text{Im}\{\gamma_l(\omega)\} \left[ \frac{\omega a}{v} \right]^{2l} K_m^2 \left[ \frac{\omega b}{v} \right], \quad (7.1)$$

where  $K_m(x)$  stand for the modified Bessel functions.  $\gamma_l(\omega)$  are the sphere surface response functions defined as:

$$\gamma_l(\omega) = \frac{l(1 - \epsilon)}{l\epsilon + l + 1}. \quad (7.2)$$

Eq. (7.1) was first obtained by Ferrell and Echenique [95], and takes into account the contribution of all the multipolar terms of the induced potential. The dipolar ( $l = 1$ ) and quadrupolar ( $l = 2$ ) contributions agree with the expressions obtained by Schmeits [25] and Kohl [96].

Note that the dipolar term of (7.1) exhibits the same asymptotic form of (4.4), which suggests that the dipolar contribution is relevant only when the electric field  $\mathbf{E}(\omega)$  is almost uniform around the target, i.e., when the sphere radius is much smaller than the range of variation of the field,  $a \ll v\omega^{-1}$ , or when the probe travels far away from the target,  $b \gg a$ . To illustrate this point, Fig. 9(a) shows the dependence of the weight of the contribution of the first modes to the total energy loss, at a grazing incidence, for metallic spheres of a different size. The dipolar contribution is only dominant for spheres much smaller than  $v\omega_s^{-1}$ . For particles of radius  $a \sim v\omega_s^{-1}$ , many  $l$ -terms contribute with similar weight and, for very large spheres, the dipolar term becomes negligible. In this case, the probe seems an almost flat surface, so the loss spectra should not differ very much from that of the planar interface. For these spheres, the main contribution to the loss spectra arises from the high multipolar terms of (7.1). An intuitive picture is provided by considering the image charge, when the electron is close to a large sphere; the induced charge density piles up in a small region of the sphere near the probe; thus, many multipolar terms are needed to describe such a localised charge density. Furthermore, the frequency  $\omega_l$  of the  $l$ th mode is determined by the zeros of the denominator of the  $\gamma_l$  functions. For a metal they are given by:

$$\omega_l = \omega_p \sqrt{\frac{l}{2l+1}}, \quad (7.3)$$

therefore, for large values of  $l$ ,  $\omega_l \rightarrow \omega_s$ , so the shape of the loss spectra differs slightly from that corresponding to a planar surface.

Fig. 9(b) represents the contribution of the first multipolar excitations to the loss probability at grazing incidence ( $b = a$ ). Here, for small spheres, the  $l$ th mode is mostly excited, when the parameter obeys the quantisation rule:  $a\omega_l v^{-1} \sim l$ , i.e., when the sphere contains  $l$  times the plasmon wave length  $2\pi\omega_l^{-1}$ , as required to form the charge density pattern corresponding to this mode, which presents  $l$  nodes.

The asymptotic behaviour of (7.1) is given by that of the Bessel functions:

$K_m(x) \sim e^{-x}$  [19], when  $x \gg 1$  and then, at the large impact parameter,  $P(\omega) \sim \exp\{-2\omega b/v\}$ ; a dependence found in the experiments [89,5]. Note that, although all the multipolar terms present the same asymptotic behaviour, the dipolar excitation becomes the dominant one at the large impact parameter (its frequency  $\omega_1$  is the lowest one), as expected.

In the case of penetrating trajectories ( $b < a$ ), the loss probability can be calculated as in the previous case. The surface contribution to the total energy loss probability is then [97]:

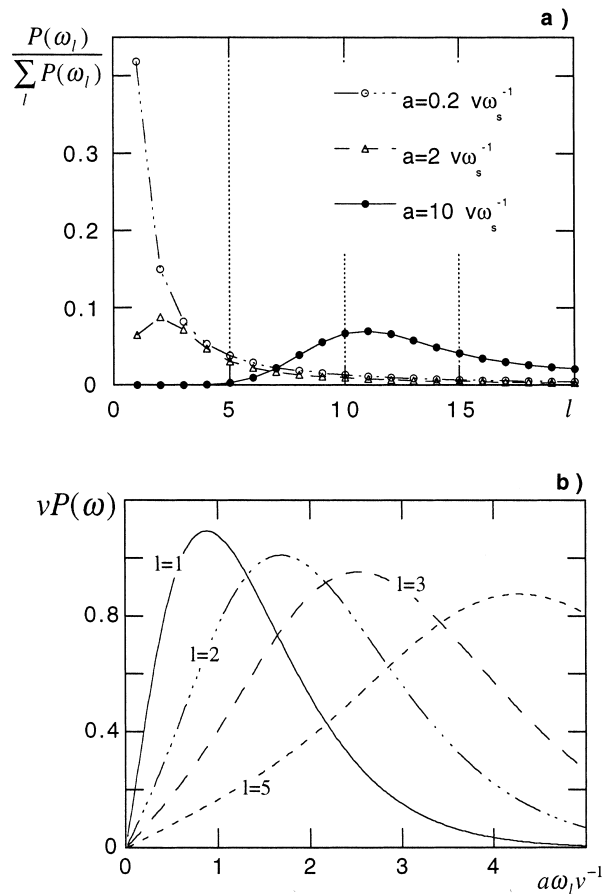


Fig. 9. (a) Relative weight of  $l$ th mode contribution to total energy loss probability experienced by electron at grazing incidence ( $b = a$ ) on Drude-like metallic sphere, for three different values of radii. (b) Contribution of first  $l$ th multipolar terms to loss probability as a function of reduced radius.

$$P_{\text{surf}}(\omega) = \frac{4a}{\pi v^2} \sum_{l=1} \sum_{m=0} (2 - \delta_{m0}) \frac{(l-m)!}{(l+m)!} \left\{ \text{Im}\{\gamma_l(\omega)\} [A_{lm}^o + A_{lm}^i]^2 + \text{Im}\left\{ \frac{1}{\epsilon(\omega)} \right\} A_{lm}^i [A_{lm}^o + A_{lm}^i] \right\}, \quad (7.4)$$

with

$$A_{lm}^o(\omega) = \frac{1}{a} \int_c^\infty dx \left\{ \frac{\sqrt{(b^2 + x^2)}}{a} \right\}^{l+1} P_l^m \left\{ \frac{x}{\sqrt{b^2 + x^2}} \right\} g_{lm} \left[ \frac{\omega x}{v} \right],$$

$$A_{lm}^i(\omega) = \frac{1}{a} \int_0^c dx \left\{ \frac{\sqrt{(b^2 + x^2)}}{a} \right\}^l P_l^m \left\{ \frac{x}{\sqrt{b^2 + x^2}} \right\} g_{lm} \left[ \frac{\omega x}{v} \right], \quad (7.5)$$

where  $c = \sqrt{a^2 - b^2}$ ,  $P_l^m(x)$  stands for Legendre functions and  $g_{lm}(x) = \cos(x)$ , if  $(l+m)$  is even, or  $\sin(x)$ , if  $(l+m)$  is odd.

Eq. (7.4) presents both terms: the surface term given by the surface response function  $\gamma_l(\omega)$  and the negative correction to the bulk loss given by the term in  $\epsilon^{-1}$ . In Fig. 10, the dependence of both terms is represented as a function of the diameter for an electron crossing axially ( $b = 0$ ) through a metallic sphere. The bulk correction is very similar to that corresponding to a film of the same thickness; both plots present the same limiting behaviours: for thick targets they both tend to the value  $P(\omega_p) \rightarrow -\pi/2v$ , whereas for  $a \rightarrow 0$  they both behave as  $t \ln(t)$ , where  $t = 2a\omega_p v^{-1}$ . From this plot, it is possible to conclude that the bulk correction is not very sensitive to the surface shape or details; it is determined basically by the thickness of the specimen. This conclusion is supported by the results obtained in reflection at the grazing incidence.

The surface loss probability is more sensitive to the surface shape; for small particles, it sends to zero, since the target vanishes in this case. In the limit of large spheres, the limit corresponding to a thick film  $P(\omega_s) \rightarrow \pi/v$  is recovered. Fig. 10 also represents the contribution of even and odd multipolar terms to the surface energy loss, where the quantisation rule, found in films (Fig. 7), is again approximately fulfilled. For the axial trajectories used in this plot, only the  $m = 0$  terms contribute, then each multipolar term  $l$  generates an induced charge density proportional to the corresponding Legendre polynomial; even (odd) modes produce a symmetric (asymmetric) surface charge distribution. This argument explains why, for very small particles ( $a \rightarrow 0$ ), the dipolar term is not the dominant one; then the time  $av^{-1} \rightarrow 0$  and, as a consequence, both poles of the sphere should be symmetrically polarised, so the dipolar contribution is zero.

In Fig. 10, the maxima and minima of both surface branches do not lie exactly at multiples of  $\pi$ , because the frequencies of the modes differ noticeably from  $\omega_s$ . The maxima and minima of each multipolar contribution satisfies exactly the condition  $2a\omega_l v^{-1} = n\pi$  ( $n$  having the same parity of  $l$ ), but since the frequency of the modes is different, the sum of all the terms shows the nodes shifted.

This study has been extended to deal with voids [98], spheroids [99] and coated spheres [89,100]. The above features of the impact parameter dependence remain valid, although the modes for these geometries are modified in value, depending on the parameters characterising each particular geometry.

### 7.2. Supported particles

From the pioneering experiments of Batson [2,3], it became evident that the theoretical model of an isolated sphere did not fully explain the experimental results. First, the energy loss peak at Al spheres appeared at lower energies than the theoretical value, and this energy shift could not be explained by the presence of an oxide coating. On the other hand, the energy loss spectra depended strongly on the supporting surface and on the beam position relative to the support.

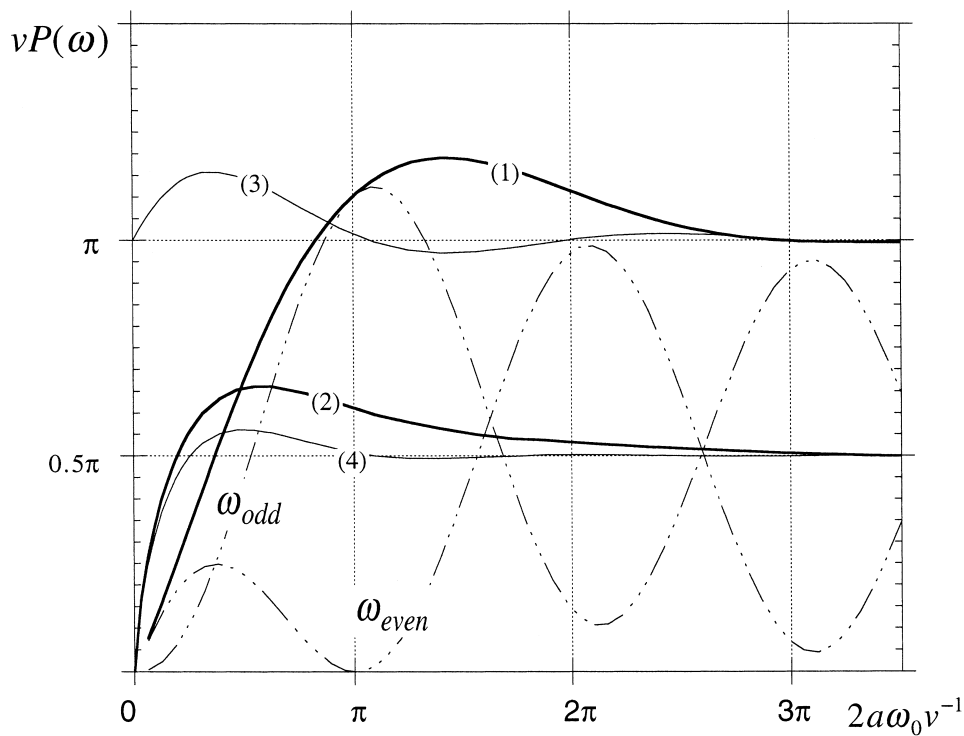


Fig. 10. Surface energy loss probability and correction to bulk energy loss probability as a function of reduced diameter  $2a\omega_0v^{-1}$ , for electron crossing axially through metallic sphere. Curves (1) and (2) correspond to surface loss probability and bulk correction, respectively. Surface contributions of even and odd multipolar terms are labelled as  $\omega_{even}$  and  $\omega_{odd}$ . Plot for a film of the same thickness has been included for comparison [curves (3) and (4)]. The energy  $\omega_0$  is  $\omega_s$  and  $\omega_p$  in surface and bulk plots, respectively. Drude dielectric function has been used. Sign of bulk corrections have been changed to fit it into plot.

Following [101], we present a simple theoretical approach to this problem; the supported particle is modelled as a metallic sphere of radius  $a$  half-embedded in a planar surface. We assume both particle and support to have the same dielectric response, and the electron to move parallel to the plane at impact parameter  $b > a$ . Applying the self-energy formalism, the screened interaction is written as that of the planar interface, plus the contribution of the sphere, which is expanded in terms of the spherical harmonics. The boundary conditions of Poisson's equation then lead to a set (one for each value of the azimuthal number  $m$ ) of algebraic linear systems coupling all the expansion coefficients with the same value of  $m$ . These systems are numerically solved and, once the screened interaction is obtained, the contribution of the particle to the energy loss probability can be computed by means of (5.8).

We focus on the impact parameter dependence of the loss spectra, for an Al particle, supported by an Al surface. Fig. 11 depicts the spectra calculated for two different positions of the beam. Above 9 eV, the spectrum of Fig. 11(a) is rather similar to that of an isolated sphere. The main difference between both spectra is that, in the case of the supported particle, the dipolar peak is shifted down. The new peak at 6.8 eV presents the same shape and intensity as the dipolar one, but due to the coupling with the support it has now a monopolar character, i.e., the surface of the particle is charged with a charge density of the same sign. The extinction of the dipolar peak is a consequence of the coupling. In a sphere, the dipolar mode piles up surface charge asymmetrically placed at opposite sides of the sphere, therefore, when the particle is embedded in a metal this mode is not allowed, and the energy of the corresponding mode is now because the charge density in the hemisphere only couples with a charge of the same sign. The monopolar character of this loss peak is experimentally confirmed by its absence, when the supporting medium is an insulator.

When the electron travels near a corner, the main feature of the spectra (Fig. 11(b)) consists of some broad resonances above the planar surface plasmons  $\omega_s$ , which is consistent with the modes of an edge [102]. The charge density corresponding to these modes consists of charges of the same sign on both surfaces, the particle and the plane, near the edge. Because there is no screening, the coupling between the charge density at both sides of the edge now raises the energy of these modes in relation to  $\omega_s$ . In the spectra corresponding to the embedded particle in Fig. 11, the energy loss probability becomes negative in the neighbourhood of 10.7 eV ( $\omega_s$ ). The negative value arises from the fact that we are just considering the particle contribution to the energy loss probability. We then have to add the contribution from the plane (dashed line in Fig. 11(a)) which has a loss peak at  $\omega_s$  that balances the negative contribution of the particle.

Fig. 12 shows the dependence of the coupling between the particle and planar surfaces on the radius of the sphere, by looking at the intensity of the peak at 6.8 eV. This coupling is a maximum when  $0.5\pi a \sim v\omega^{-1}$ , i.e., when the distance between the probe and the edge along the surface is of the order of the adiabatic length  $v\omega^{-1}$ . For larger values, the edge, and, therefore, the coupling, is outside the range of the potential, and its influence is negligible.

Experimental observations by Batson [2,3] on Al particles confirm qualitatively the validity of these results. He found an anomalous low-energy peak (around 4 eV) was present (absent) when the particles were supported in another larger Al particle (insulator,  $\text{AlF}_3$ ). On the other hand, the dependence of this peak on the impact parameter is similar to that theoretically found.

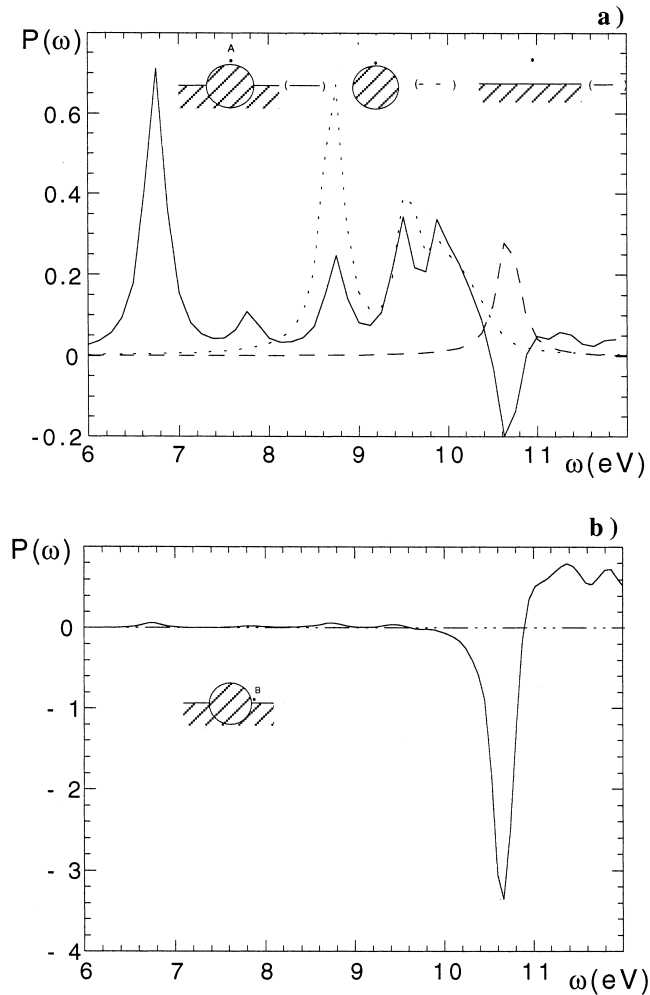


Fig. 11. Particle contribution to loss spectra corresponding to Al sphere half-embedded in Al support for two different beam positions (solid lines). Radius is 10 nm. (a) Beam is at position labelled A and distance from top of the sphere to beam is 1 nm. Spectra corresponding to same beam position near isolated sphere (dotted line) and planar interface of length  $2a$  (dashed line). (b) Beam at position B. Distance between beam and both surfaces is 1 nm. Drude dielectric function with small damping has been used ( $\omega_p = 15.1$  eV,  $\gamma = 0.27$  eV).

A better quantitative agreement requires a more realistic geometric model of the target, by taking into account the oxide coating present in experimental situations [101], as well as a better modelling of the supporting surface.

### 7.3. Hemispherical particles

In many experimental situations, small particles are supported on a substrate, when performing experiments. Due to the presence of the support, the particles often show different geometric shape, such as the hemispherical one. Ouyang et al. [94] have reported very accurate experimental data for the size dependence of the surface loss peak energy of STEM electrons interacting with nearly hemispherical Ag particles lying on a C surface. The high energy resolution of these data (about 0.1 eV), and the fact that the silver surface is clean and oxide-free, make a good test from this experiment of the applicability of the classical dielectric theory to describe the surface excitations. The authors found that the energy of the loss peak shifts down from the expected small particle value, as the radius of the particles decreases in the range of 4–10 nm, presenting a minimum value  $\omega \sim 3.2$  eV for particles of about 4 nm. For smaller particles, the energy of the peak then grows to reach the value 3.8 eV, but for such small particles, the dielectric theory is no longer suitable. The loss peak energies, found in this region, agree with the data obtained from optical absorption measurements, which have been theoretically explained by the quantum many-body theory [103,104]. On the other hand, in the range of 4–10 nm, the dielectric theory is supposed to provide a good description of the particle excitations. Nevertheless, by using optical values of the dielectric function [105], it is easy to prove that the behaviour of the EELS for

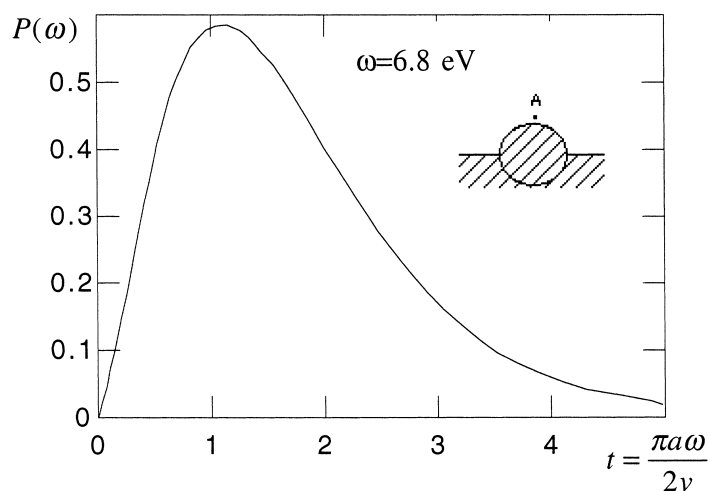


Fig. 12. Dependence of height of the 6.8 eV peak with reduced radius of particle. The beam is at position labelled A and distance from top of sphere to the beam is 1 nm.

particles of this size cannot be explained in terms of the excitations of a sphere, since the Ag surface plasmon energies move from the dipolar value  $\omega_1 = 3.5$  eV to the planar one  $\omega_s = 3.65$  eV, values well above the experimentally found energies. Relativistic corrections are expected to be negligible for such small particles, since the parameter  $a\omega c^{-1}$  is too small ( $\sim 5 \cdot 10^{-2}$ ).

A theoretical study of these results has been reported [107]. The particles are considered as hemispheres, and the problem is handled as discussed in the previous section, using experimental values of the dielectric function. Fig. 13(a) and (b) shows the theoretical energy loss spectra corresponding to an Ag hemisphere of a different radius;  $a = 5$  and 40 nm, respectively, for different beam positions. It can be seen that two dominant loss peaks appear around 3.2 and 3.6 eV. The former is a characteristic resonance of the hemispherical geometry. The charge density corresponding to this resonance basically depends on the azimuthal angle  $\phi$  as  $\cos \phi$ , i.e., near the edge, charges of the same sign are piled in front on both the hemispherical and planar surfaces, in a configuration somewhat similar to that of the film symmetric model  $\omega_+$ . Its corresponding charge density presents a strong dipolar pattern which is responsible for the predominance of this mode, when the STEM beam travels far away from the hemisphere. On the other hand, in the 3.6 eV mode, the coupling between both surfaces is not so strong and its corresponding charge density is similar to that of a plane or large sphere. This charge density distribution explains the fact that, when the probe travels close to the top of the particle (position A), the 3.6 eV is the dominant excitation, while the low energy peak at 3.2 eV is more relevant for electron trajectories close to the corner (position C). For intermediate beam positions (B), the 3.6 eV peak is the dominant contribution to the spectrum corresponding to the large particle, since, at this position, the probe sees an almost planar surface ( $v\omega^{-1} \sim a$ ), while in the spectrum of the small particle the dominant feature is the 3.2 eV peak. This observation explains the experimental results, the low energy peak is the dominant one in the case of small particles, while for the large particles its contribution is very small and the spectrum is centred at 3.6 eV. Note that the 3.2 eV peak is also present in the experimental data corresponding to large particles.

Wang and Cowley [65,168–170] have presented experiments with Al hemispherical particles lying in  $\text{AlF}_3$ . Their EELS also presented two peaks, which can be explained as above. The impact parameter dependence agrees qualitatively with the former discussion.

#### 7.4. Relativistic effects in small particles

The problem of the relativistic energy loss, experienced by a fast electron passing near or across a small particle, is much more complex than that of the case of a planar target. The radius  $a$  introduces a new length scale in the retarded interaction. Furthermore, radiative losses become possible [108].

The standard way to find the solution for an electron impinging on a target consists of writing the electric and magnetic fields in terms of the dyadic GF of

the Helmholtz equation. For a sphere, the GF is written as an expansion in a proper basis, which in the case of a spherical surface, is found to be products of Bessel functions and spherical harmonics. The coefficients of this expansion are calculated to fulfil the boundary conditions of the electric and magnetic fields at the interface [109,171,53]. The electromagnetic modes correspond to the

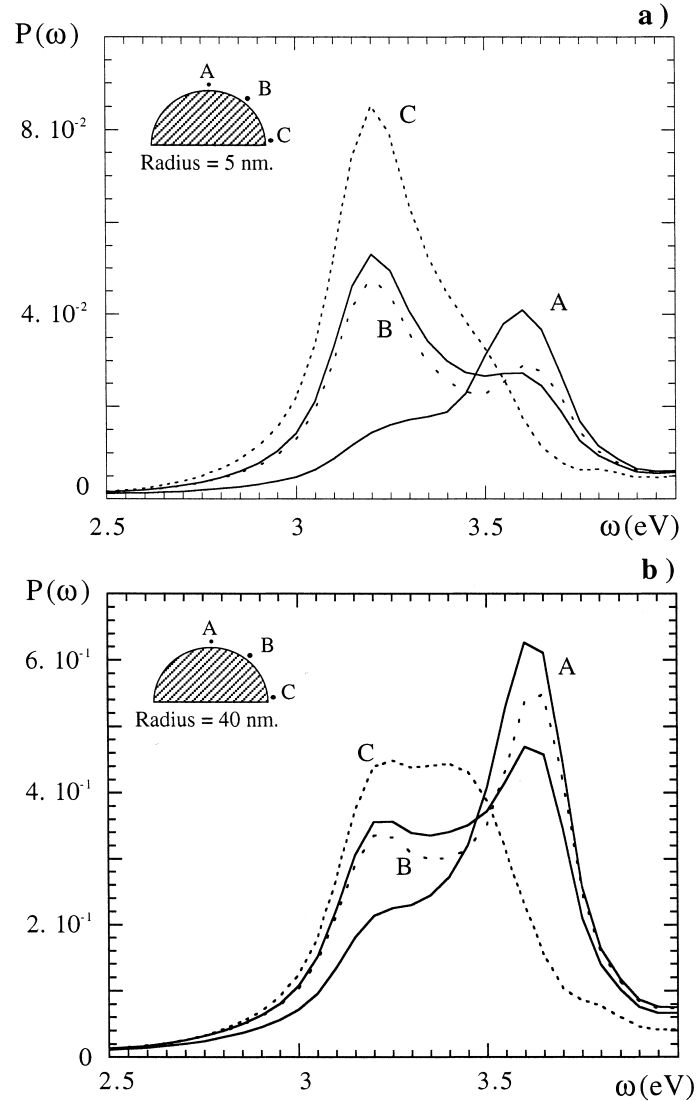


Fig. 13. Energy loss spectra for Ag hemispheres and different electron trajectories, labelled A, B, C. In (a) hemisphere radius  $a = 5$  nm, and in (b)  $a = 40$  nm.

frequencies for which Maxwell equations present non-trivial solutions, when there is no external current. For a sphere, the electromagnetic modes were studied by Fuchs and Kliewer (polariton modes) [55] and by Ruppin (plasmonic modes) [56]. The frequency of these modes depends only on the parameter  $a\omega_p/c$ , a fact that confirms that the effect of the retardation derives from the coupling of the charge density; the interaction time is of the order of  $ac^{-1}$  (for the dipolar term), a time to compare with the plasmon period.

Fig. 14(a) shows the modes of a metallic sphere as a function of the dimensionless parameter  $a\omega_p/c$ . The frequency of the dipolar mode is severely shifted down, even for particles of the order  $a \sim c\omega_p^{-1}$ . For high multipolar excitations, this effect is weaker because their corresponding charge density presents more nodes and the charge density coupling occurs at shorter distances. Note that the non-retarded values given by (7.3) are recovered as  $a\omega_p/c \rightarrow 0$ .

For an electron travelling close to a particle, once the electric field is obtained, the electron energy loss probability can be calculated, as in the non-retarded case, as the work done by the induced electric field acting back all along the probe trajectory  $\mathbf{r}=\mathbf{v}t$ . To evaluate this effect, we present the energy loss spectra corresponding to a fast electron travelling close to a dielectric sphere of radius,  $a$ , for non-penetrating trajectories ( $b > a$ ). In Fig. 14(b), we compare retarded and non-retarded EELS, for two spheres of a different radius,  $a = 5$  nm ( $a\omega_p v^{-1} \sim 0.4$ ) and  $a = 10$  nm. As expected, the relativistic effects become more important as the particle radius grows; the dipolar excitation presents a red shift for both radii, whereas the high multipolar contribution is almost unchanged. On the other hand, in the retarded spectra, the dipolar peak intensity is slightly lower, as found for the planar interface (see Fig. 3). The shifting in the dipolar peak corresponds to that shown in Fig. 14(a). The broadening of the dipolar peak is connected with an additional channel of radiative decay of the surface plasmons [59,132]. One can conclude that near the surface, the non-retarded approximation is accurate for particles of the order of  $a \sim 0.5c/\omega_p$  ( $a \sim 7$  nm in the case of an Al particle with  $\omega_p = 15.8$  eV).

### 7.5. Many-particle systems

EELS has been applied to the study of inhomogeneous media, such as colloids and zeolites. In these problems, the emphasis focused on the general properties of the composite, rather than in particular details of its constituents. One way of gaining insight into such a complex geometry is to concentrate on the system formed by just two coupled particles. Different theoretical works have attempted to explain such results, by considering simple models to compute the energy losses corresponding to complex targets, as a couple of spherical particles [110] or two cylinders [111]. Recently, several sum rules relating the modes of two non-touching coupled surfaces to those of the decoupled ones have appeared [112], in order to provide a general insight into the collective excitations in coupled surfaces. In general, as the geometry of the target shows a more detailed structure,

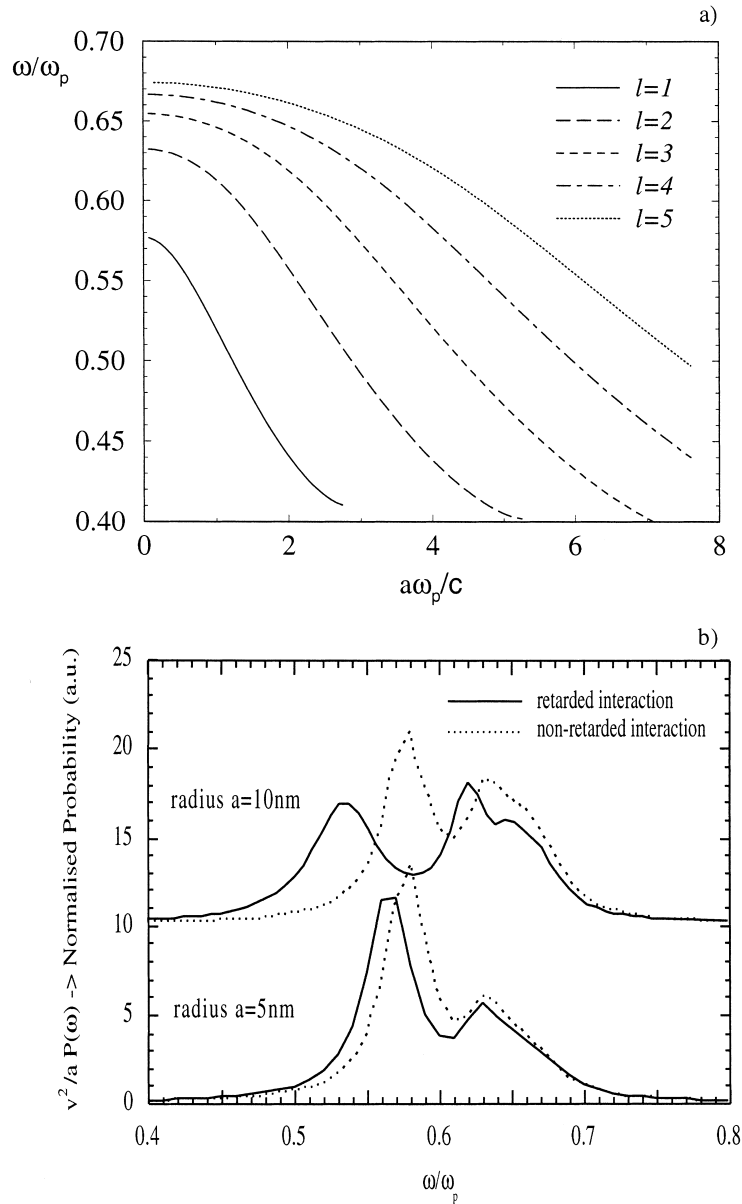


Fig. 14. (a) Frequency of retarded modes corresponding to metallic sphere in units of plasma frequency  $\omega_p$ . (b) Electron energy loss probability (normalised to size of the particle  $a$ ) for 100 keV electron travelling close to particles of radius  $a = 5$  and 10 nm. Retarded case (solid lines) is compared to non-retarded case (dashed lines). Probabilities have been shifted 10 units, in order to clarify the plot. Impact parameter is  $b = a + 1$  nm. Drude dielectric function has been used ( $\omega_p = 15.8$  eV,  $\gamma = 0.53$  eV).

it becomes considerably more difficult to obtain analytical expressions and more computation time is usually required to find the energy loss probability.

The first treatments of collective excitations in systems of two spheres [113,114,110] only considered the contribution of the first multipolar terms. A more general solution, valid for any dielectric function and any trajectory, has been recently reported [115], computing the energy loss probability in the framework of the self-energy formalism. The screened interaction is written in bispherical coordinates, so that the excitations produced by different electron trajectories around and between the spheres can be studied, as well as their dependence on the particle size and on the distance between spheres. In general, many multipolar terms are needed to secure good convergence.

In Fig. 15, calculated loss spectra for Al particles in an  $\text{AlF}_3$  matrix are shown. For trajectories labelled C and F, the polarisation pattern of both spheres can roughly be described as that corresponding to two parallel dipoles. As discussed before, the coupling of both dipoles in an insulating medium tends to lower the energy of the system in relation to that of the uncoupled spheres. When the probe travels at the position D, it induces a symmetric charge density in both spheres, so the energy of the system increases. This last case is similar to that of a particle moving between two semi-infinite metallic media. These arguments also explain the dependence of the energy of these modes on the parameter  $x = a/d$ , where  $a$  and  $d$  are the particle radius and interparticle distance: the larger the ratio  $x$ , the more effective the coupling between charge density and, therefore, the larger the shifting of the energy.

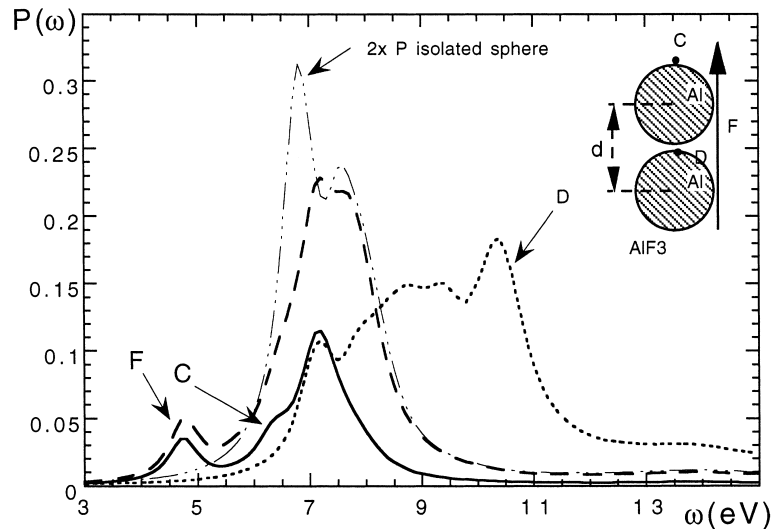


Fig. 15. Calculated EELS spectra for electrons travelling near two close Al spheres of radius  $r = 10$  nm and ratio  $x = a/d = 0.48$  immersed in  $\text{AlF}_3$ . Experimental dielectric functions have been used [106].

The different resonances appearing in the spectra are related to the structure and intensity of the induced electric field around the particles. Even for less close particles, the field is shown to be very localised in the space between the particles ( $x = a/d \simeq 0.4$ ), which is in agreement with the predictions of Pendry's theory, where the energy-loss calculation near a semi-infinite colloidal medium, modelled as a cubic lattice of spherical particles, showed that the loss spectrum was not significantly modified by including more than two particle arrays [117].

The application of the *boundary charge method* (BCM) (Appendix B) enables more than two spheres, constituting an array, to be considered. Comparison between EELS in the two and infinite arrays has also been performed. Fig. 16 provides the calculated EELS spectra for a three Al particle array in an  $\text{AlF}_3$  host. The probability per sphere, in a system of three spheres, has been considered by varying the distance in between,  $d$ , i.e., the filling fraction of the system  $x = a/d$ . The main contribution to the losses is due to the particle–host interaction (*dipolar peak*) and the sphere–sphere interaction (*coupling peak*).

For high filling fractions ( $x = 0.48 \propto 46\%$ ), the coupling peak is shifted down to 4.5 eV, which is lower than that of the vacuum ( $\sim 6$  eV). As the filling fraction of the system decreases, the high energy peaks are maintained and even enhanced

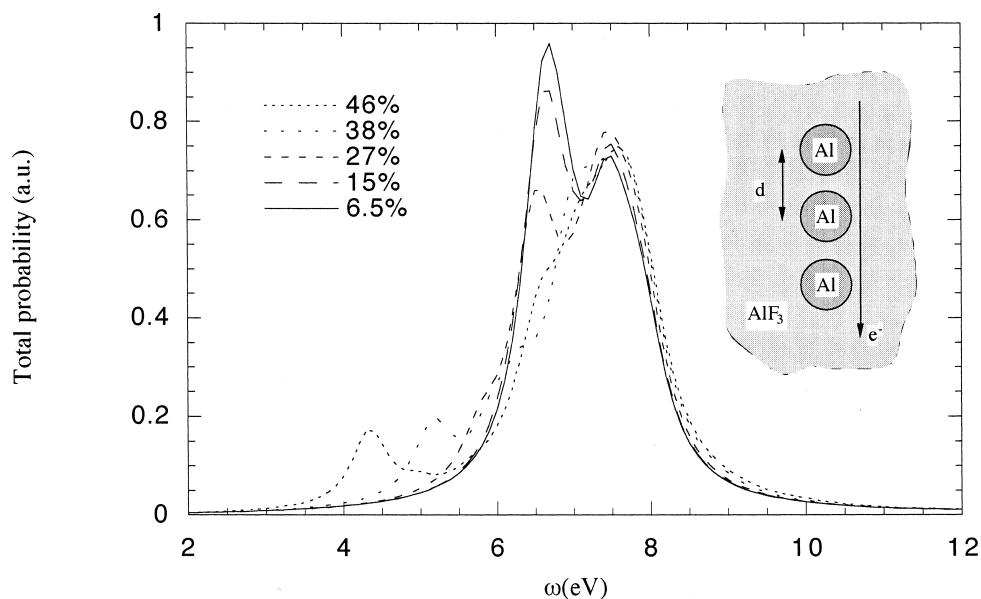


Fig. 16. Energy loss probability suffered by 100 keV electrons moving parallel to the system of three Al spheres aligned along direction of motion of electrons. Difference distance between sphere  $d$  corresponds to different filling fractions in colloidal situation ( $x = a/d$ ). Al spheres are surrounded by  $\text{AlF}_3$ . Spheres are 10 nm radius and electron trajectory is parallel to the arrow axis, at distance of 1 nm from spherical surfaces. Experimental values of dielectric function of  $\text{AlF}_3$  have been used [116].

(dipolar peak at least) and the low energy peak disappears, recovering the spectrum features of an Al isolated sphere embedded in  $\text{AlF}_3$ .

Coupled spheres are of interest, both in their own right and in the context of a many-sphere medium, as a correction to effective medium theories, in which the inverse of the dielectric function of the system is calculated as an average related to the microstructure and properties of its constituents [118,117,119]. In most experiments in inhomogeneous media, the situation is difficult to undertake, since the beam crosses particles of different sizes in an irregular distribution. Kaiser et al. [120] investigated a system consisting of small Au particles in an  $\text{SiO}_2$  matrix, and concluded that the *Maxwell–Garnett theory* (MGT) [121] is only valid for very dilute media. Howie and Walsh [66], by studying Al colloids in  $\text{AlF}_3$ , concluded that classical effective medium theories of this kind are not completely successful in explaining the energy loss spectra observed, but much better results are obtained with a dielectric excitation model, making an average over the possible electron trajectories in the composite medium. The main point is that the MGT only includes the dipolar surface loss and the bulk loss of the surrounding medium. It does not include the bulk loss of the spheres, which is considerable for  $a\omega/v > 1$ . The chief drawback of the effective medium theories arises from replacing an inhomogeneous medium by an equivalent homogeneous one, with the resulting risk of losing effects related to very local excitations around the inhomogeneities of the material, which can give important contributions to the EELS spectra.

Two recent papers have tackled these problems from different points of view. Pendry and Martin-Morena [117] developed a formulation, very well suited for numerical calculation, which consists of calculating the energy loss rate by integration of the Poynting vector, corresponding to the reflected field in systems constituted by arrays of spheres. They calculated the energy loss for an electron moving past a surface, considering the medium below the surface as inhomogeneous, but ordered (arrays of metal spheres or cylinders), so that a transfer-matrix method [118] could be used to obtain the Poynting vector from the reflectance amplitude. Barrera and Fuchs [119] considered a random system of spherical particles in a host, characterising both media by their local dielectric functions and calculating the energy loss spectrum from the effective inverse longitudinal dielectric response obtained as an average over particle positions. They recover the MG dielectric function as the  $q = 0$  limit of that function.

## 8. Cylindrical surfaces

The pioneering investigation of plasmon excitations in cylindrical surfaces were motivated by light reflection experiments [122] in the early 1970s. Ashley and Emerson [123] and Pfeiffer et al. [124] then obtained the dispersion relations for surface plasmons on cylindrical surfaces by considering the retarding effects of the electromagnetic fields. Martinos and Economou [125] studied the plasmon excitations in cylindrical surfaces by electrons describing circular orbits around

cylinders, moved by axial magnetic fields. Warmack et al. [126] obtained the first energy loss spectrum in microchannels of 20–200 nm drilled in metallic films and Chu et al. [127] provided the estimate of the energy loss probability of electrons moving in cylindrical channels in the non-relativistic approximation, to account for the energy loss suffered by electrons in particle accelerators. Interest in the cylindrical geometry increased in the 1980s, due to the ability shown by the STEM electron beam to drill holes and lines of nanometre size in films of about 100 nm thick of inorganic materials [128–130], such as alumina or aluminium fluoride. These experiments opened great expectations for the use of a STEM beam as a nanometre scale pen, of great interest in microelectronics and nanolithography. The EELS technique permits the study of chemical changes that take place during the drilling process. It was also pointed out [130,129,9] that a metallisation process can occur during the drilling process.

Expressions for the energy loss in clean and metal-coated holes have been reported by Walsh [57] and Sabala et al. [58] to study the damage process. But the colloidal nature of the metallic inclusions seems to be better described through an effective medium theory as proposed by Howie and Walsh [66]. De Zutter and De Vleeschauwer [131] studied the retarded expression in the axial trajectory of the electron, which has also been generalised for a general impact parameter [58]. In the previous works, local dielectric functions have been used to describe the medium. A general calculation, including the momentum dependence of the dielectric function that describes the medium surrounding the cylindrical cavity, has also appeared [132]. A general formulation of the energy loss probability in cylindrical surfaces, valid for any electron trajectory, has also been reported [133], within the framework of the quantal self-energy formalism. The *begrenzung* features for different penetrating trajectories were also analysed. The effects of the coupling between micropores in the loss spectra were analysed by Schmeits [111].

Earlier treatments considered probes of electrons travelling on a definite trajectory, and only very recently a broad-beam configuration has been used to study the energy loss probability in cylindrical surfaces [77], so as to give account of STEM experiments in nanotubes where the size of the beam is comparable to the beam width. In this decade, the discovery of tubular fullerenes [134] gave rise to a new and very promising field of application of these theories. The research on the properties of these new nanostructures were pursued by efforts from different experimental techniques [135], including EELS. Spatially resolved EELS was performed on individual single wall [136] and multiwall carbon nanotubes [137–139]. Pichler's recent EELS experiment proved the metallic character of potassium intercalated carbon nanotubes. The collective excitations in carbon nanotubes have also been studied theoretically [140–144]. Recently, Reed et al. [145] applied the EELS technique to the study of Si tips and filaments.

An effective dielectric function, for systems of cylinders, has been obtained in order to investigate the valence loss spectra in zeolites [146]. Very recently, nanoscale-size fibres have been studied by EELS with non-penetrating electrons [147], as well.

The expression for the energy loss probability of an electron travelling in a

cavity of radius  $a$  in a material characterised by its local dielectric function at an impact parameter  $b$  related to the axis of the hole is

$$P(\omega) = \frac{2}{\pi v^2} \sum_{m=0}^{\infty} (2 - \delta_{m0}) I_m^2(B) \operatorname{Im} \left\{ \frac{K_m(A) K_m'(A) [\epsilon(\omega) - 1]}{\xi_m} \right\}, \quad b < a \quad (8.1)$$

and

$$P(\omega) = \frac{2}{\pi v^2} \sum_{m=0}^{\infty} (2 - \delta_{m0}) K_m^2(B) \operatorname{Im} \left\{ \frac{I_m(A) I_m'(A) [\epsilon(\omega) - 1]}{\epsilon(\omega) \xi_m} \right\}, \quad b > a, \quad (8.2)$$

with  $\xi_m = I_m(A) K_m'(A) \epsilon(\omega) - I_m'(A) K_m(A)$ .  $I_m(x)$  and  $K_m(x)$  are the modified Bessel functions with arguments  $A = \omega a/v$  and  $B = \omega b/v$ . Note that for axial trajectories ( $B = 0$ ) the probability is due exclusively to the  $m = 0$  mode. The probabilities corresponding to a wire of the same radius are obtained by interchanging  $\epsilon$  by  $\epsilon^{-1}$  in (8.1) and (8.2).

Fig. 17 shows dispersion curves of the first modes of a hole (a) and a wire (b), where  $q$  is the component of the momentum parallel to the cylinder axis. For parallel trajectories,  $q = \omega/v$ . The energies of all the modes are quite close to the planar surface plasmon energy,  $\omega_s$ , except for  $m = 0$ . This difference can be explained by looking at the induced charge density. The contribution of the  $m$ -mode to the induced charge density depends on the azimuthal angle  $\phi$  as  $\cos(m\phi)$ , so the  $m = 0$  mode corresponds to a homogeneous charge distribution around the cylindrical surface. For the wire, the  $m = 0$  mode shifts downwards from the planar surface plasmon energy as the radius is decreased. In this case, the charge density coupling is similar to that found for the symmetric mode  $\omega_-$  in films. For the hole, its energy shifts from the bulk plasmon energy  $\omega_p$ , for a small hole radius towards the planar surface plasmon, for a large radius. In this case, the induced charge coupling is through a vacuum, leading to this blue shift. For large values of the radius ( $qa > 1$ ), all the modes tend to the same energy and at an impact parameter close to the interface, the planar limit is obtained [58]. Expressions for coated cylinders have also appeared in the literature to simulate the damage during the drilling process [57,58]. Retarded expressions have been evaluated and proved to be considerable for wide holes and energies, such that  $\operatorname{Re}(\epsilon(\omega)) > c^2/v^2$ .

## 9. EELS in complex configurations: truncated nanostructures

Edged structures, such as MgO cubes, have been widely used to study the probe–surface interaction. Nevertheless, most of the experiments were performed at the grazing incidence and the samples were large enough to justify the neglect of the edge effects [28,29,31]. The use of EELS, as a technique to investigate nanostructures of interest in microelectronics, has attracted increasing attention to the specific features of this geometry in edged samples, such as films and interface junctions.

Theoretical studies of modes and plasmon frequencies in cubes, rectangular particles and wedges have been reported [148–151]. Recently, the energy of the loss peak in an Si–SiO<sub>2</sub> interface, has been studied [152]. Deducing the loss spectrum for such complex geometries requires the calculation of the induced potential; it poses a challenging computational problem which has been

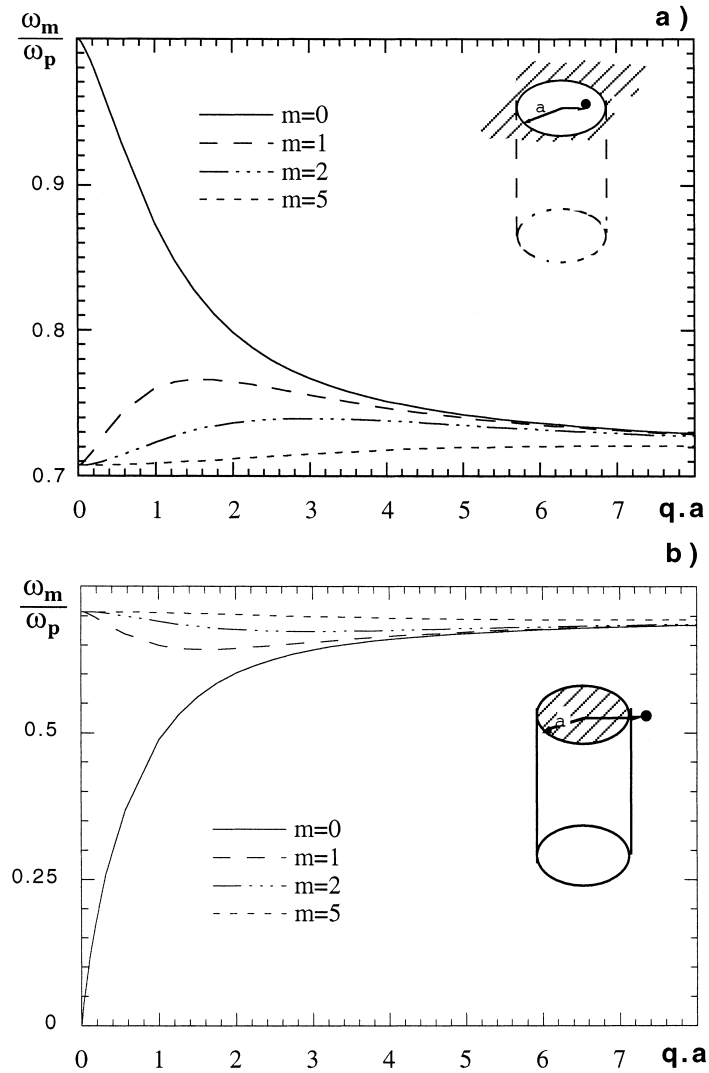


Fig. 17. Energy of first surface plasmon modes in (a) cylindrical cavity in aluminium and (b) aluminium wire, as a function of its reduced radius  $qa$ .

successfully tackled via the BCM (see Appendix B). The results of this section prove the power of this approach [153].

To work out the geometry in the case of a  $90^\circ$  wedge, the target is modelled as a surface of a hyperbolic cross section in the  $xy$ -plane normal to the edge, i.e.,  $y=p^2/(2x)$ , so that  $p$  is the distance from the surface vertex to the origin and the asymptotes of the hyperbola coincide with the  $x$ - and  $y$ -axes, as in Fig. 18.

Fig. 18(a) and (b) represents the evolution of the loss of spectra (normalised to the path length) as the electron beam sweeps a line parallel to a very sharp edge. For trajectories near to position A, the spectra are similar to that of the infinite plane; they basically present the surface peak at  $\omega_s$  (plus the negative begrenzung term at  $\omega_p$ , in the case of inner trajectories). They also feature some very weak peaks at energies below and above  $\omega_s$ , which constitute the edge effect. The intensity of these peaks increases as the trajectory moves closer to the edge; becoming the dominant feature in the spectra for trajectories close to the edge.

The BCM provides a simple way to evaluate the  $\omega$ -component of the induced charge density. In Fig. 19, we plot the charge density corresponding to the first pair of symmetric and antisymmetric modes. The modes with an energy smaller

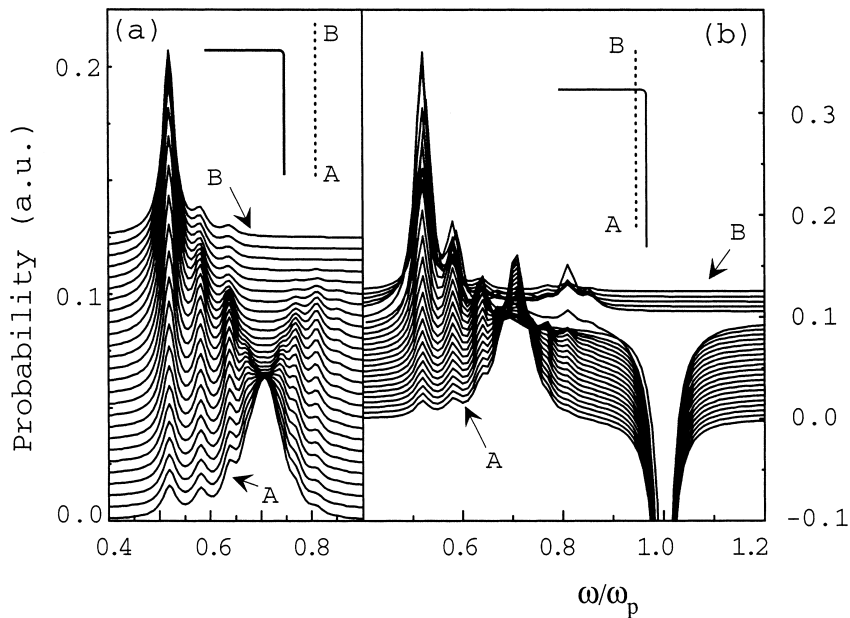


Fig. 18. Dependence of energy loss per unit path length  $P(\omega)$  on beam position for trajectories parallel to edge. Different spectra correspond to equally separated positions of beam, as in inset. Spectra are scanned between both ends of those lines designated A and B, respectively, and whose coordinates (relative to the vertex) are (in a.u.)  $(50, -200)$  and  $(50, 50)$  in (a) and  $(-20, -200)$  and  $(-20, 50)$  in (b), respectively. Electron travels in vacuum in (a) and inside wedge for some trajectories in (b). Edge is very sharp  $p = 0.01 \text{ a.u.} \ll v\omega^{-1}$ . Energy of beam is 100 keV and Drude dielectric function has been used ( $\omega_p = 15.8 \text{ eV}$ ,  $\gamma = 0.5 \text{ eV}$ ).

(larger) than  $\omega_s$  correspond to a symmetric (antisymmetric) charge density distribution on both faces of the edge. As discussed, in the case of the thin film, this shift results from the coupling between the charge distribution of both faces, which are screened by a dielectric function that is negative in this energy range. Therefore, in the case of symmetric mode, it tends to lower the energy.

As a test of this theory, we calculate the edge effect in an MgO cube so as to compare with observed spectra. The cube in the experiment is 100 nm large, a length that makes the coupling between edges ( $100 \text{ nm} \sim 10v\omega^{-1}$ ) negligible, therefore, the previous calculation can be realistic. Experimental values of the dielectric function are used. In Fig. 20, we present both the STEM observed energy loss spectrum and the total calculated energy loss probability  $P(\omega)$ , for two different positions of the beam. Both plots agree, in absolute terms, to a factor of about 0.7. Since the exact position of the edge is uncertain in all experimental situations, there can be a bulk contribution at 22 eV, due to some beam penetration of the cube. The simulation does not reproduce the excitations experimentally observed in the band gap region (below 7 eV), which must arise, either from defects, or from relativistic effects. In this case, the beam is travelling 1 nm just inside the edge and the contribution of the 22 eV bulk loss appears

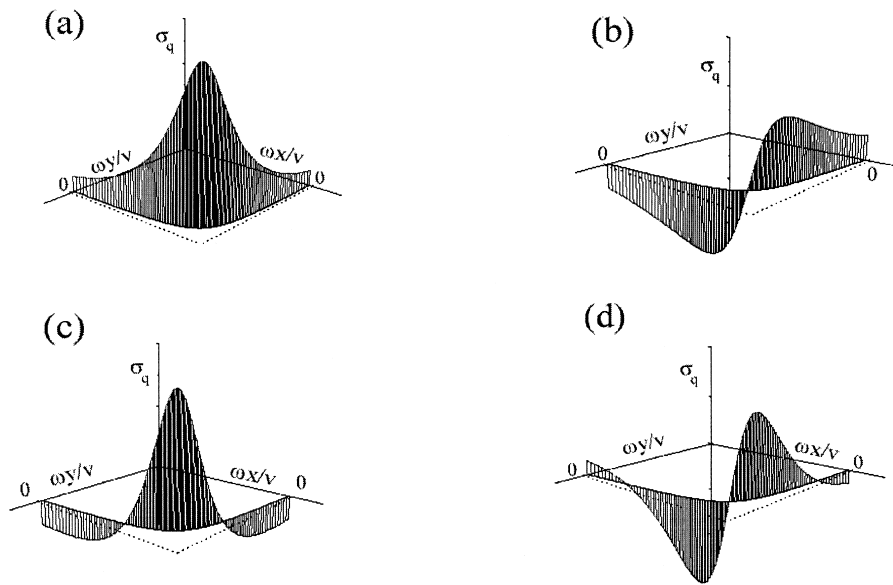


Fig. 19. Charge densities corresponding to the first two edge modes below and above  $\omega_s$ . The first pair (a) and (b) correspond to the corner peaks at  $\omega \sim 0.52\omega_p$  and  $\omega \sim 0.58\omega_p$  and the second pair (c) and (d) correspond to the energy loss peaks at  $\omega \sim 0.84\omega_p$  and  $\omega \sim 0.79\omega_p$ . To make the plot clearer, the parameter  $p$  has been taken as  $p \sim 0.1v/\omega_p^{-1}$ ; this change produces a small shift of the energies in relation to those of the spectra in Fig. 18.

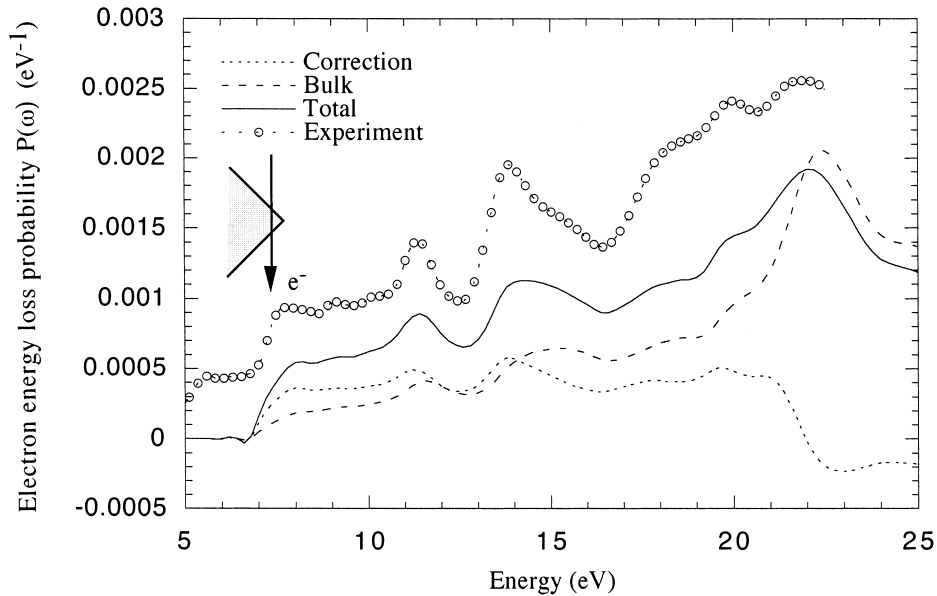


Fig. 20. Energy loss probability  $P(\omega)$  for 100 keV electron impinging on MgO cube as in inset. Plots labelled as “correction” and “bulk” are total surface contribution, and bulk direct term. Impact parameter relative to the vertex is 1 nm.

together with the other excitations from the top and bottom surfaces, as well as from the edge.

This study has been extended to deal with many other problems frequently encountered in experiments, such as that of a thin slab containing two different dielectric regions separated by a boundary running normal to the slab surfaces, and other different junctions, where the effect of sharp boundaries is a dominant feature [132,154].

## 10. Conclusions

In this work, the image potential has been proved to provide an accurate description of the inelastic scattering of fast electrons with surfaces. The excitation of bulk and surface plasmons, due to the target–probe interaction, has been analysed. In most experimental STEM situations, classical and quantal descriptions of the beam electrons lead to the same result for the energy loss probability. The energies of surface plasmons are basically determined by the target geometry. The spatial resolution of EELS experiments is given by the length scale  $v\omega^{-1}$ , which provides the spatial extension of the region, where the coupling between surfaces takes place. The relativistic corrections have been evaluated for planes and spherical particles and have proved to be crucial for

large targets of large impact parameters. On the other hand, for very small impact parameters, a momentum-dependent dielectric function is needed to provide a good description of EELS spectra. Methods developed to account for the energy loss in nanostructures of increasing complexity have been described as well.

### Acknowledgements

We wish to express our sincere thanks to Profs A. Howie, P. M. Echenique, R. Ritchie and P. Apell for many stimulating suggestions and discussions during the preparation of the manuscript. The work of Dr F. J. García de Abajo concerning the BCM method was of great help. We are also indebted to Profs R. García-Molina and P. E. Batson for providing valuable references and data. The authors also thank the Basque Government for financial support (PI-1997-39).

## Appendix A

### Dielectric response function

In the dielectric formalism all the information about the target excited by an external probe is contained in the *dielectric function*, which, in principle, depends on both momentum  $\mathbf{q}$  and energy  $\omega$ . For a homogeneous electron gas,  $\epsilon(\mathbf{q}, \omega)$  can be obtained from the time-dependent perturbation theory [155]. Knowledge of this function provides a great deal of information. In fact, it gives directly the response of the system to weak external time and space varying longitudinal fields, the density fluctuation excitation spectrum, both single-particle and collective excitations, etc. In 1954, Lindhard [156] obtained an explicit expression for this response function using the so-called *random phase approximation* (RPA) approximation in which the electrons are supposed to respond independently to the external fields, i.e., exchange and correlation effects between electrons are not included. In the RPA, the response function is related to the free-electron polarisability  $\alpha_0(\mathbf{q}, \omega)$  as

$$\epsilon(\mathbf{q}, \omega) = 1 + 4\pi\alpha_0(\mathbf{q}, \omega). \quad (\text{A1})$$

This *dielectric function* describes both the collective and individual properties of the electron gas by avoiding the damping  $\gamma$  of the electronic oscillations. In 1970, Mermin [37] modified this function to account for the damping. Approximations of these expressions have proved to describe the properties of the electron gas quite well. One of the most commonly used is the *plasmon-pole approximation* [157,67,158], in which

$$\epsilon(\mathbf{q}, \omega) = 1 + \frac{\omega_p^2}{\beta^2 q^2 + \frac{q^4}{4} - \omega(\omega + i\gamma)}, \quad (\text{A2})$$

where  $\beta^2 = \frac{3}{5}v_F^2$  and  $v_F$  is the Fermi velocity. In the null-damping limit,  $\gamma \rightarrow 0$ , this function gives the plasmon dispersion relation for small  $q$ , and for large  $q$ , it tends to the one electron energy-momentum relation  $\omega = q^2/2$ . In the loss function, it gives a sharp peak corresponding to the bulk-plasmon energy that moves slightly towards higher energies with increasing momentum. Besides this, there is a broad structure corresponding to the electron–hole pair excitations. For high momenta, the plasmon oscillations are damped, since one plasmon can transfer its energy to an electron, producing an electron–hole pair. From energy conservation considerations, the critical  $q$  to produce such pairs is quoted [155] as  $q_c \sim (\omega_p/v_F)$ . When one is only interested in the collective excitations of the electron gas, the momentum dependence of the dielectric response function can often be avoided, and reduced to the *optical approximation*  $\epsilon(\mathbf{q}=0, \omega)$ . The simplest model of dielectric response, which accounts for the behaviour of a metal, is the well-known *Drude dielectric function* that considers free electrons with a damping constant  $\gamma$ , so

$$\epsilon(\omega) = 1 - \frac{\omega_p^2}{\omega(\omega + i\gamma)}. \quad (\text{A3})$$

For this dielectric function, the *loss function* is a Lorentzian, centred at  $\omega_p$  and with a width given by the damping,

$$\text{Im} \left[ \frac{-1}{\epsilon(\omega)} \right] = \frac{\omega_p^2 \omega \gamma}{(\omega^2 - \omega_p^2)^2 + \omega^2 \gamma^2}, \quad (\text{A4})$$

which, in the undamped limit, yields the simple expression

$$\lim_{\gamma \rightarrow 0} \text{Im} \left[ \frac{-1}{\epsilon(\omega)} \right] = \frac{\pi}{2} \omega_p \delta(\omega - \omega_p). \quad (\text{A5})$$

The above theoretical dielectric functions are simple models describing an electron gas or ideal metal. The *experimental dielectric function*  $\epsilon(\omega)$  provides more detailed information about the response of the medium, and compares much better to the experimental results. This function is usually obtained from optical data, by measuring the reflectance in a large range of frequencies [105]. Another way of obtaining it is by means of the EELS in transmission experiments. Making the acceptance angle very small, one can obtain the *energy-loss spectra* corresponding to  $q = 0$ . These spectra are proportional to the loss function  $\text{Im}\{-\epsilon(\omega)^{-1}\}$ . Provided the loss function is known over a wide interval, from the Kramers–Kronig relations, it is possible to obtain the real and imaginary parts of the dielectric function [12,159].

## Appendix B

### Methods of solving the Poisson equation

Here we consider the following Fourier transform convention:

$$f(\mathbf{k}, \omega) = \int_{-\infty}^{\infty} d\mathbf{r} \int_{-\infty}^{\infty} dt e^{-i(\mathbf{k}\mathbf{r}-\omega t)} f(\mathbf{r}, t),$$

$$f(\mathbf{r}, t) = \frac{1}{(2\pi)^4} \int_{-\infty}^{\infty} d\mathbf{k} \int_{-\infty}^{\infty} d\omega e^{i(\mathbf{k}\mathbf{r}-\omega t)} f(\mathbf{k}, \omega). \quad (\text{B1})$$

A useful approach to calculate the energy loss of a probe near a surface is through the so-called *screened interaction*, or GF of the Poisson equation (2.1), i.e., it is the solution of the equation:

$$\nabla^2 W(\mathbf{r}, \mathbf{r}', \omega) = \frac{-4\pi}{\epsilon(\omega)} \delta(\mathbf{r} - \mathbf{r}'), \quad (\text{B2})$$

which verifies the same boundary conditions as the solution of (2.1), i.e., the screened interaction  $W(\mathbf{r}, \mathbf{r}', \omega)$  and  $\epsilon \partial W(\mathbf{r}, \mathbf{r}', \omega)/\partial n$ , where  $\partial/\partial n$  stands for the normal derivative, should be continuous on the interfaces. The solution of (2.1) can be straightforwardly written in terms of  $W(\mathbf{r}, \mathbf{r}', \omega)$  as:

$$\phi(\mathbf{r}, \omega) = \int_{-\infty}^{\infty} d\mathbf{r}' W(\mathbf{r}, \mathbf{r}', \omega) \rho(\mathbf{r}', \omega). \quad (\text{B3})$$

In situations where the surface presents a simple geometric shape, a simple way to calculate  $W(\mathbf{r}, \mathbf{r}', \omega)$  is to interpret it formally as the Poisson equation corresponding to a point charge at rest at  $\mathbf{r}'$ , and then solve it by the standard techniques of the electrodynamics.

As an example of this method, we obtain the potential created by an electron moving with constant velocity parallel to a planar interface, as discussed in Section 2. The standard way of tackling problems involving planar interfaces (planes, films, multilayers) is by means of a Fourier transformation of (B2) and solving it in the  $k$ -space. Nevertheless, for a simple planar interface, the solution can be easily obtained by noticing that the solution of (B2) is formally the same as that of the static image potential in a medium of dielectric “constant”  $\epsilon(\omega)$  [18]. The screened interaction is then given by:

$$W(\mathbf{r}, \mathbf{r}', \omega)$$

$$= \frac{1}{|\mathbf{r} - \mathbf{r}'|} - \frac{\xi(\omega)}{\sqrt{(x - x')^2 + (y - y')^2 + (z + z')^2}}, \quad z, z' > 0$$

$$= \frac{1}{\epsilon(\omega)} \frac{1}{|\mathbf{r} - \mathbf{r}'|} - \frac{\xi(\omega)}{\sqrt{(x - x')^2 + (y - y')^2 + (z + z')^2}}, \quad z, z' < 0 \quad (\text{B4})$$

$$= -\frac{\xi(\omega) - 1}{\sqrt{(x - x')^2 + (y - y')^2 + (z - z')^2}}, \quad z, z' < 0,$$

where  $x$ ,  $x'$ , etc. ... are the cartesian coordinates of  $\mathbf{r}$  and  $\mathbf{r}'$ , respectively. The functions  $\xi(\omega)$  and  $\zeta(\omega)$  are given by (2.4) and (2.15), respectively. These terms contain the surface contribution to the screened interaction.

For trajectories outside and parallel to the surface, the charge density is given by (2.2); combining this expression with (B3) one can write the induced potential as:

$$\phi_{\text{ind}}(\mathbf{r}, \omega) = \frac{\zeta(\omega)}{v} \int_{-\infty}^{\infty} dx' \frac{e^{i\frac{\omega x}{v}x'}}{\sqrt{(x-x')^2 + y^2 + (z+b)^2}} \quad (\text{B5})$$

and then, by using the integral representation of the Bessel function  $K_0(x)$  [19]:

$$K_0[|x|] = \int_0^{\infty} \frac{\cos(xt)}{\sqrt{1+t^2}} dt, \quad (\text{B6})$$

we have the induced term of (2.3).

The first terms in the screened interaction (when both  $z$  and  $z' > 0$ ) lead to the direct Coulomb potential  $\phi_{\infty}$ , which corresponds to the solution of Poisson equation in a non-bounded medium. Applying (B3) to this term, we find:

$$\phi_{\infty}(\mathbf{r}, \omega) = -2\frac{Z}{v} K_0 \left\{ \frac{|\omega|}{v} \sqrt{y^2 + (z-b)^2} \right\} e^{i\frac{\omega x}{v}}, \quad (\text{B7})$$

which can be generalised for the bulk term (when both  $z$  and  $z' < 0$ ); the corresponding expression just differs in the  $\epsilon^{-1}$  factor. Returning to (B7), we see it is  $\omega$ -independent, so can be straightforwardly a Fourier transform to obtain

$$\phi_{\infty}(\mathbf{r}, t) = \frac{-1}{\sqrt{(x-vt)^2 + y^2 + (z-b)^2}}, \quad (\text{B8})$$

where we have used the following result [19]:

$$\int_0^{\infty} dx \cos(bx) K_0(x) = \frac{\pi}{2} \frac{1}{\sqrt{1+b^2}}. \quad (\text{B9})$$

Eq. (B8) states an obvious result: it is the Coulomb potential created by a charge moving in a vacuum.

In many problems, the *energy loss probability* can be directly obtained from the screened interactions via (5.8), without obtaining the induced potential. As an example, we apply this method to obtain the EELS for an electron travelling outside a dielectric sphere. We expand the induced part of the screened interaction  $W_{\text{ind}}(\mathbf{r}, \mathbf{r}', \omega)$  as a regular solution of the Laplace equation in each region of the space, the coefficients of this expansion are then calculated by imposing the boundary conditions. The screened interaction can be written as [72]:

$$\begin{aligned}
W(\mathbf{r}, \mathbf{r}', \omega) &= \sum_{l, m} \frac{4\pi}{2l+1} \gamma_l(\omega) \frac{a^{2l+1}}{(r, r')^{l+1}} Y_{lm}^*(\Omega') Y_{lm}(\Omega) + \frac{1}{|\mathbf{r} - \mathbf{r}'|} \quad r, r' > a \\
&= \sum_{l, m} \frac{4\pi}{2l+1} \{\gamma_l(\omega) + 1\} \frac{r'^l}{r^{l+1}} Y_{lm}^*(\Omega') Y_{lm}(\Omega) \quad r < (a, r') < a \\
&= \sum_{l, m} \frac{4\pi}{2l+1} \left\{ \gamma_l(\omega) + 1 - \frac{1}{\epsilon(\omega)} \right\} \frac{(r, r')^l}{a^{2l+1}} Y_{lm}^*(\Omega') Y_{lm}(\Omega) \\
&\quad + \frac{1}{\epsilon(\omega)} \frac{1}{|\mathbf{r} - \mathbf{r}'|} \quad r, r' < a,
\end{aligned} \tag{B10}$$

where  $r < (r >)$  is the smallest (greatest) of  $r$ , and  $r'$  and  $Y_{lm}(\Omega)$  are their corresponding spherical harmonic functions. The response functions  $\gamma_l(\omega)$  are given by (7.2). Note that the Coulomb terms in these expressions can be expanded as [18]:

$$\frac{1}{|\mathbf{r} - \mathbf{r}'|} = \sum_{l, m} \frac{4\pi}{2l+1} \frac{r'^l}{r^{l+1}} Y_{lm}^*(\Omega') Y_{lm}(\Omega). \tag{B11}$$

Once the screened interaction is known, the *energy loss probability* can be calculated from (5.8). For non-penetrating electron trajectories, we recover (7.1) easily. In this step, the following non-trivial result is needed [160]:

$$\int_{-\infty}^{\infty} dx \frac{P_l^m \left\{ \frac{x}{\sqrt{b^2 + x^2}} \right\}}{(\sqrt{b^2 + x^2})^{l+1}} e^{ikx} = 2 \left\{ \frac{ik}{|k|} \right\}^{l-m} \frac{|k|^l}{(l-m)!} K_m(|k|b). \tag{B12}$$

For penetrating trajectories,  $b < a$ , one can proceed as above. In this case, one has to be aware of the fact that the direct bulk term  $\epsilon^{-1}/|\mathbf{r} - \mathbf{r}'|$  (for  $r, r' < a$ ) is boundary dependent, since it is only defined inside the sphere. This term then provides not only the non-bounded medium bulk term, but also part of the *begrenzung* contribution. This term has to be obtained by writing it as the contribution of an infinite medium, proportional to the path length inside the sphere, plus a surface correction to the bulk term.

This is a simple application of the standard method of solving Poisson's equation; it consists, basically, of writing the induced potential or the screened interaction  $W(\mathbf{r}, \mathbf{r}', \omega)$  as a linear combination of the solutions to the Laplace equation. The problem then reduces to finding the complex coefficients of this combination: the application of the boundary conditions leads to a set of algebraic linear equations involving these coefficients. Planes, films, spheres, cylinders and spheroids have been solved in a simple way. In the most complicated cases — two spheres or two cylinders, particle coupled

to a plane — all the coefficients are coupled, so, a cut-off in the number of functions used in the expansion has to be imposed, which leads to complicated computational problems. In these last problems, (5.8) has been proved to be computationally advantageous, because it simply reduces the problem to solving a double integral.

The existence of such a basis implies high symmetry in the target geometry; as the target geometry complicates, this method becomes unsuitable, since it is not possible to choose a single basis of functions, where the boundary conditions can be analytically handled. At this stage, direct computation is required. The BCM has been proposed to deal with this problem [153]. This approach can be traced back to Maxwell, who used it to compute capacitances [161]. It has been employed much more recently, to determine the normal-mode frequencies of dielectric excitations of a cube by Fuchs [162,163] and by Ouyang and Isaacson for bodies of arbitrary shape [164]. Ouyang and Isaacson [165] proceeded to apply the boundary method to investigate the effect of the support on fast electron energy losses near small particles. Other recent applications of this approach include the surface modes of channels cut on planar surfaces [166] and those of coupled parallel wires [167]. Although the previous works are not referenced, this method has been used very recently by Reed et al. [145]. A generalisation of this procedure, including relativistic corrections, has also been presented [59].

We are again faced with solving the Poisson equation (2.1) in the local approach for a given external charge density  $\rho(\mathbf{r}, \omega)$  and given boundary conditions. However, instead of solving it directly in terms of a field defined in a three-dimensional space (the induced potential), the BCM reduces the problem to finding the surface charge density  $\sigma(\mathbf{s}, \omega)$  induced by the external charge density, and writing the induced field in terms of this magnitude. This unknown field  $\sigma(\mathbf{s}, \omega)$  is now defined on a two-dimensional support. In addition, the boundary conditions are implemented in the equation for the charge density.

This method is of general use in problems involving probes and surfaces, as far as the local dielectric response approach is valid. It has been successfully used in EELS in electron microscopy. Here, for simple targets (plane, sphere, cylinder, etc.), when it is possible to handle analytically the charge density, the well-known formulae are recovered. Semi-analytical computation for systems consisting of many ordered spheres have been developed, where the charge density of each sphere is written in terms of its spherical harmonics, and the coefficients then numerically computed.

Nevertheless, the main interest of this technique is its ability of dealing with very complex boundaries. The fact that the charge density is defined just on the surfaces, allows one to deal numerically with it by defining its values at the discrete points of a grid.

We now describe briefly the theoretical basis of this method. A detailed exposition can be found in [153]. In an inhomogeneous system, where the dielectric function changes abruptly at the interfaces, the Poisson equation enables the total charge density on the interface,  $\sigma(\mathbf{s}, \omega)$ , to be related to the normal

component of the electric field:

$$\sigma(\mathbf{s}, \omega) = \frac{1}{4\pi} [\mathbf{E}_{\text{out}}(\mathbf{s}, \omega) - \mathbf{E}_{\text{in}}(\mathbf{s}, \omega)] \mathbf{n}_{\mathbf{s}}, \quad (\text{B13})$$

where  $\mathbf{s}$  is the coordinate vector running over the interfaces,  $\mathbf{E}_{\text{out}}(\mathbf{s}, \omega)$  and  $\mathbf{E}_{\text{in}}(\mathbf{s}, \omega)$  are the electric field inside and outside the surface and  $\mathbf{n}_{\mathbf{s}}$  is the interface normal at  $\mathbf{s}$  pointing towards the outer medium. Note that, in the general case, the distinction between the inner and outer medium is arbitrary, and the convention used here has to be followed throughout. When there is no free charge on the interface, the normal component of the electric displacement is continuous on the interface and the function  $\sigma(\mathbf{s}, \omega)$  is now the induced charge density. It is then possible to write the charge density as a function of the normal component of the electric field:

$$\sigma(\mathbf{s}, \omega) = \frac{1}{4\pi} \frac{\epsilon_{\text{in}} - \epsilon_{\text{out}}}{\epsilon_{\text{in}}} \mathbf{E}_{\text{out}}(\mathbf{s}, \omega) \mathbf{n}_{\mathbf{s}}, \quad (\text{B14})$$

where  $\epsilon_{\text{out}}$  and  $\epsilon_{\text{in}}$  are the dielectric functions of both media. From the Gauss theorem, the normal component of the electric field near the surface can be written as the sum of the contribution of the field  $\mathbf{E}_{\text{ext}}$  created by all the external charges, plus the contribution of the charge density:  $\mathbf{n}_{\mathbf{s}} \mathbf{E}_{\text{out}}(\mathbf{s}, \omega) = \mathbf{n}_{\mathbf{s}} \mathbf{E}_{\text{ext}}(\mathbf{s}, \omega) + 2\pi\sigma(\mathbf{s}, \omega)$ . Eq. (B14) then becomes

$$\Lambda(\omega)\sigma(\mathbf{s}, \omega) = \mathbf{n}_{\mathbf{s}} \mathbf{E}_{\text{ext}}(\mathbf{s}, \omega) = \mathbf{n}_{\mathbf{s}} \mathbf{E}_{\text{probe}}(\mathbf{s}, \omega) \mathbf{n}_{\mathbf{s}} + \int ds' F(\mathbf{s}, \mathbf{s}') \sigma(\mathbf{s}', \omega), \quad (\text{B15})$$

where

$$\Lambda(\omega) = 2\pi \frac{\epsilon_{\text{out}}(\omega) + \epsilon_{\text{in}}(\omega)}{\epsilon_{\text{out}}(\omega) - \epsilon_{\text{in}}(\omega)}. \quad (\text{B16})$$

In (B15), the external field at the surface,  $\mathbf{E}_{\text{ext}}$ , has been written as the sum of the field created by the external probe (whatever it is)  $\mathbf{E}_{\text{probe}}$ , plus that created by the surface density. This last contribution is given by the integral over the surface in (B15), where

$$F(\mathbf{s}, \mathbf{s}') = -\frac{\mathbf{n}_{\mathbf{s}}(\mathbf{s} - \mathbf{s}')}{|\mathbf{s} - \mathbf{s}'|^3} \quad (\text{B17})$$

is the electric field created by the unit charge at  $\mathbf{s}'$  in the point  $\mathbf{s}$ . Note that, although this term diverges as  $\mathbf{s} \rightarrow \mathbf{s}'$ , its contribution remains finite, since the electric field becomes normal to the surface, so  $\mathbf{n}_{\mathbf{s}}(\mathbf{s} - \mathbf{s}') \rightarrow 0$ . This requires that the surface is smooth; nevertheless, it is possible to use this model with edged surfaces by smoothing out the corner up to a distance much smaller than the length involved in the problem [153].

Expression (B15) is an integral equation, which relates the values of the induced surface density to the field created by the external probes. When the surface is

simple enough to allow an analytical expansion of the charge density, this equation reduces to a set of linear equations relating the coefficients of this expansion. In more complex geometries, the charge density has to be defined by means of its values at discrete points  $\mathbf{s}_i$  of a grid over the surface, and then, this equation leads to a system of linear equations coupling all the values of  $\sigma(\mathbf{s}_i, \omega)$ .

Once the charge density is known, we can derive from it any physical magnitude; for instance, the induced potential can be straightforwardly obtained as:

$$\phi_{\text{ind}}(\mathbf{r}, \omega) = \int d\mathbf{s} \frac{\sigma(\mathbf{s}, \omega)}{|\mathbf{r} - \mathbf{s}|}. \quad (\text{B18})$$

The contribution of the surface terms to the energy loss probability  $P_{\text{surface}}(\omega)$  can be expressed in terms of the induced potential, when this is evaluated at the electron position, in the standard way:

$$P_{\text{surf}}(\omega) = \frac{-2}{\pi v} \int d\mathbf{s} K_0 \left[ \frac{\omega |\mathbf{r}_0^\perp - \mathbf{s}^\perp|}{v} \right] \text{Im} \{ \sigma(\mathbf{s}, \omega) e^{i(r_0^\parallel - s^\parallel)\omega/v} \}. \quad (\text{B19})$$

When there is no external probe, (B15) becomes a useful way of obtaining the modes of complex surfaces, characterised by a Drude dielectric function. The energies of the modes are given by

$$\Lambda(\omega)\sigma(\mathbf{s}, \omega) - \int d\mathbf{s}' F(\mathbf{s}, \mathbf{s}')\sigma(\mathbf{s}', \omega) = 0. \quad (\text{B20})$$

If one transforms (B20) into a linear system, the modes are the values of  $\omega$  for which the matrix of the system is singular. Note that this fact implies that this method is no longer valid to deal with such a dielectric function. The use of a small damping in  $\epsilon(\omega)$  theoretically avoids this problem, but one has to be aware of the computational difficulties, when inverting a near singular matrix. Nevertheless, this problem does not occur, when using experimental dielectric functions.

## References

- [1] G. Rutherman, *Ann. Phys.* 2 (1948) 113.
- [2] P.E. Batson, *Ultramicroscopy* 9 (1982) 227.
- [3] P.E. Batson, *Phys. Rev. Lett.* 49 (1982) 936.
- [4] P.E. Batson, *Ultramicroscopy* 11 (1983) 229.
- [5] D. Ugarte, C. Colliex, P. Trebbia, *Phys. Rev. B* 45 (1992) 4332.
- [6] C.C. Ahn, O.L. Krivanek, *EELS Atlas*, Gatan Inc and Arizona State University, 1983.
- [7] D. Bohm, D. Pines, *Phys. Rev.* 82 (1951) 625.
- [8] R.H. Ritchie, *Phys. Rev.* 106 (1957) 874.
- [9] S.D. Berger, J. Bruley, L.M. Brown, D.R. McKenzie, *Ultramicroscopy* 28 (1989) 43.
- [10] M.G. Walls, A. Howie, *Ultramicroscopy* 28 (1989) 40.
- [11] H. Petersen, *Solid State Commun.* 23 (1977) 931.

- [12] R.F. Egerton, *Electron Energy-Loss Spectroscopy in Electron Microscope*, Plenum Press, New York, 1996.
- [13] H. Raether, *Excitation of Plasmons and Interband Transitions by Electrons*, Springer-Verlag, Berlin, 1980.
- [14] H. Raether, Surface plasmons on smooth and rough surfaces and on gratings, in: *Springer Tracts in Modern Physics*, vol. 111, Springer-Verlag, Berlin, 1988.
- [15] P. Schattschneider, *Fundamentals of Inelastic Electron Scattering*, Springer-Verlag, Berlin, 1986.
- [16] Z.L. Wang, *Elastic and Inelastic Scattering in Electron Diffraction and Imaging*, Plenum Press, New York, 1995; *Micron* 27, 265, 1996.
- [17] N. Takimoto, *Phys. Rev.* 146 (1966) 366.
- [18] J.D. Jackson, *Classical Electrodynamics*, Wiley, New York, 1975.
- [19] M. Abramowitz, I.A. Stegun, *Handbook of Mathematical Functions*, Dover, New York, 1964.
- [20] P.M. Echenique, J.B. Pendry, *J. Phys. C* 8 (1975) 2936.
- [21] C.J. Powell, J.B. Swan, *Phys. Rev.* 118 (1960) 640.
- [22] R. Nuñez, P.M. Echenique, R.H. Ritchie, *J. Phys. C* 13 (1980) 4229.
- [23] A. Howie, R.H. Milne, *Ultramicroscopy* 18 (1985) 427.
- [24] D. Pines, D. Bohm, *Phys. Rev.* 8 (1952) 338.
- [25] M. Schmeits, *J. Phys. C* 14 (1981) 1203.
- [26] A. Howie, *Ultramicroscopy* 11 (1983) 141.
- [27] J.P. Muscat, D.M. Newns, *Surf. Sci.* 64 (1977) 641.
- [28] L.D. Marks, *Solid State Commun.* 43 (1982) 727.
- [29] J.M. Cowley, *Surface Sci.* 114 (1982) 231.
- [30] A. Howie, R.H. Milne, *J. Microsc.* 136 (1984) 279.
- [31] R.H. Milne, P.M. Echenique, *Solid State Commun.* 55 (1985) 909.
- [32] N. Barberán, P.M. Echenique, J. Viñas, *J. Phys. C* 12 (1979) L111.
- [33] P.M. Echenique, R.H. Ritchie, N. Barberán, J. Inkson, *Phys. Rev. B* 23 (1981) 6486.
- [34] P.M. Echenique, *Philos. Mag. B* 52 (1985) L9.
- [35] N. Zabala, P.M. Echenique, *Ultramicroscopy* 32 (1990) 327.
- [36] F.J. García de Abajo, P.M. Echenique, *Phys. Rev. B* 45 (1992) 8771.
- [37] N.D. Mermin, *Phys. Rev. B* 1 (1970) 2362.
- [38] R.H. Ritchie, A.L. Marusak, *Surf. Sci.* 4 (1966) 234.
- [39] R.H. Ritchie, A. Howie, *Philos. Mag. A* 36 (1977) 463.
- [40] D.R. Penn, *Phys. Rev. B* 35 (1987) 482.
- [41] J.C. Ashley, *J. Elec. Spect. Rel. Phen.* 46 (1988) 199.
- [42] P.E. Batson Proc. 38th EMSA, San Francisco, 1980. p. 124.
- [43] P.E. Batson, M.M.J. Treacy Proc. 38th EMSA, San Francisco, 1980. p. 126.
- [44] P.M. Echenique, A. Howie, *Ultramicroscopy* 16 (1985) 269.
- [45] C.S. Tan, J.M. Cowley, *Ultramicroscopy* 12 (1983) 333.
- [46] A. Rivacoba, P.M. Echenique, *Ultramicroscopy* 26 (1988) 389.
- [47] Torregrosa A. Martínez, R. García-Molina, *Ultramicroscopy* 34 (1990) 283.
- [48] R.H. Ritchie, H.B. Eldridge, *Phys. Rev.* 126 (1962) 1935.
- [49] A. Otto, *Phys. Stat. Sol.* 22 (1967) 101.
- [50] E. Kröger, *Z. Phys. A* 235 (1970) 403.
- [51] R. García-Molina, A. Gras-Martí, A. Howie, R.H. Ritchie, *J. Phys. C* 18 (1985) 5335.
- [52] R.H. Ritchie, *Surf. Sci.* 34 (1973) 1.
- [53] J.A. Stratton, *Electromagnetic Theory*, McGraw-Hill, New York, 1941.
- [54] P. Moreau, N. Brun, C.A. Walsh, C. Colliex, A. Howie, *Phys. Rev. B* 56 (1997) 6774.
- [55] R. Fuchs, K.L. Kliewer, *J. Opt. Soc. Am.* 58 (1968) 319.
- [56] R. Ruppin, in: A.D. Boardman (Ed.), *Electromagnetic Surface Modes*, Wiley, Chichester, 1982, p. 345.
- [57] C.A. Walsh, *Philos. Mag. A* 59 (1989) 227.
- [58] N. Zabala, A. Rivacoba, P.M. Echenique, *Surf. Sci.* 209 (1989) 465.
- [59] F.J. García de Abajo, A. Howie, *Phys. Rev. Lett.* 80 (1998) 5180.
- [60] R.H. Ritchie, *Philos. Mag. A* 44 (1981) 931.

- [61] O.L. Krivanek, A.J. Gubbens, N. Delby, C.E. Mayer, *Microsc. Microanal. Microstruct.* 3 (1992) 187.
- [62] D.W. McComb, A. Howie, *Ultramicroscopy* 34 (1990) 84.
- [63] R.H. Ritchie, A. Howie, *Philos. Mag. A* 58 (1988) 753.
- [64] P.E. Batson, *Ultramicroscopy* 47 (1992) 133.
- [65] Z.L. Wang, J.M. Cowley, *Ultramicroscopy* 21 (1987) 77.
- [66] A. Howie, C.A. Walsh, *Microsc. Microanal.* 2 (1991) 171.
- [67] L. Hedin, S. Lundquist H. Ehrenreich, D. Turnbull, editors. *Solid State Physics*. Academic New York, 1969. vol. 29. p. 1.
- [68] F. Flores, F. García-Moliner, *J. Phys. C* 12 (1979) 907.
- [69] P.J. Feibelman, C.B. Duke, A. Bagchi, *Phys. Rev. B* 5 (1972) 2436.
- [70] P.M. Echenique, F. Flores, in: P.M. Echenique (Ed.), *Electrones en materia condensada. Interaccion de cargas y radiacion con la materia*, UPV-EHU, San Sebastian, 1988.
- [71] J.R. Manson, R.H. Ritchie, *Phys. Rev. B* 24 (1981) 4867.
- [72] P.M. Echenique, J. Bausells, A. Rivacoba, *Phys. Rev. B* 35 (1987) 1521.
- [73] A. Rivacoba, N. Zabala, P.M. Echenique, *Phys. Rev. Lett.* 69 (1992) 3362.
- [74] J.C. Inkson, *Many-body Theory of Solids*, Plenum Press, New York, 1984.
- [75] P.M. Echenique, J.B. Pendry, *Prog. Surf. Sci.* 32 (1989) 111.
- [76] L.I. Schiff, *Quantum Mechanics*, McGraw-Hill, Singapore, 1968.
- [77] J.M. Pitarke, A. Rivacoba, *Surf. Sci.* 377 (379) (1997) 294.
- [78] D.R. Penn, P. Apell, *J. Phys. C* 16 (1983) 5729.
- [79] L.D. Landau, E.M. Lifshitz, *Quantum Mechanics*, Pergamon, Oxford, 1977.
- [80] H. Cohen, T. Maniv, R. Tenne, Hacoheh Y. Rosenfeld, O. Stephan, C. Colliex, *Phys. Rev. Lett.* 80 (1998) 782.
- [81] P.M. Echenique, A. Howie, R.H. Ritchie, *Phys. Rev. Lett.* 83 (1999) 658.
- [82] A.A. Lucas, E. Kartheuser, *Phys. Rev. B* 1 (1985) 3588.
- [83] A. Howie, R.H. Milne, M.G. Walls A. Hilger, editors. *Proceedings of the EMAG Conference*, Bristol, 1985.
- [84] A.L. Bleloch, A. Howie, R.H. Milne, M.G. Walls, in: P.K. Larsen, P.J. Dobson (Eds.), *Reflection High-Energy Electron Diffraction and Reflection Electron Imaging of Surfaces*, Plenum Press, New York, 1988, p. 77.
- [85] A.A. Lucas, M. Sunjic, *Phys. Rev. Lett.* 26 (1971) 229.
- [86] E. Evans, D.L. Mills, *Phys. Rev. B* 5 (1972) 4126.
- [87] A. Howie, in: A. Howie, U. Valdrè (Eds.), *REM Surface and Interface Characterization by Electron Optical Methods*, Plenum Press, New York, 1988, p. 19.
- [88] Fan Cheng-Gao, A. Howie, C.A. Walsh, Tuan Jun, *Solid State Phen.* 5 (1989) 15.
- [89] P.M. Echenique, A. Howie, D.J. Wheatley, *Phil. Mag. B* 56 (1987) 335.
- [90] F. Fujimoto, K. Komaki, K. Ishida, *J. Phys. Soc. Japan* 23 (1967) 1186.
- [91] F. Fujimoto, K. Komaki, *J. Phys. Soc. Japan* 25 (1968) 1679.
- [92] P.E. Batson, *Solid State Commun.* 34 (1980) 447.
- [93] M. Achèche, C. Colliex, H. Kohl, A. Nourtier, P. Trebbia, *Ultramicroscopy* 20 (1986) 99.
- [94] F. Ouyang, P.E. Batson, M. Isaacson, *Phys. Rev. B* 46 (15) (1992) 421.
- [95] T.L. Ferrell, P.M. Echenique, *Phys. Rev. Lett.* 55 (1985) 1526.
- [96] H. Kohl, *Ultramicroscopy* 11 (1983) 53.
- [97] A. Rivacoba, P.M. Echenique, *Scann. Microsc.* 4 (1990) 73.
- [98] N. Barberan, J. Bausells, *Solid State Commun.* 73 (1990) 651.
- [99] B.L. Illman, V.E. Anderson, R.J. Warmack, T.L. Ferrell, *Phys. Rev. B* 38 (1988) 3045.
- [100] J. Bausells, A. Rivacoba, P.M. Echenique, *Surf. Sci.* 189/190 (1987) 1015.
- [101] N. Zabala, A. Rivacoba, *Phys. Rev. B* 48 (1993) 14,534.
- [102] R. García-Molina, Gras-Martí, R.H. Ritchie, *Phys. Rev. B* 31 (1985) 121.
- [103] J. Tiggesbümker, L. Klier, K. Meiwes-Broer, A. Liebsch, *Phys. Rev. A* 48 (1993) 1749.
- [104] A. Liebsch, *Phys. Rev. B* 48 (1993) 15.
- [105] E.D. Palik, *Handbook of Optical Constants of Solids*, Academic, London, 1985.
- [106] H.J. Hageman, W. Gudat, C. Kunz, *Desy Report SR 74/7* unpublished, 1974.

- [107] J. Aizpurua, A. Rivacoba, P. Apell, Phys. Rev. B 54 (1996) 2901.
- [108] R. Pogorzelski, C. Yeh, Phys. Rev. A 8 (1973) 137.
- [109] P. Morse, H. Feshbach, in: *Methods of Theoretical Physics*, McGraw-Hill, New York, 1953, pp. 745–748.
- [110] M. Schmeits, L. Dambly, Phys. Rev. B 44 (1991) 12,706.
- [111] M. Schmeits, Phys. Rev. B 39 (1989) 7567.
- [112] S.P. Apell, P.M. Echenique, R.H. Ritchie, *Ultramicroscopy* 65 (1996) 53.
- [113] A.A. Lucas, A. Ronveaux, M. Schmeits, F. Delanaye, Phys. Rev. B 12 (1975) 7567.
- [114] R. Ruppim, Phys. Rev. B 26 (1982) 3440.
- [115] N. Zabala, A. Rivacoba, P.M. Echenique, Phys. Rev. B 56 (1997) 7623.
- [116] C.A. Walsh, Ph.D. thesis, University of Cambridge, 1987.
- [117] J.B. Pendry, L. Martín-Moreno, Phys. Rev. B 50 (1994) 5062.
- [118] J.B. Pendry, A. MacKinnon, Phys. Rev. Lett. 69 (1999) 2772.
- [119] R.G. Barrera, R. Fuchs, Phys. Rev. B 52 (1995) 3256.
- [120] W.J. Kaiser, E.M. Logothetis, L.E. Wenger, J. Phys. C 18 (1985) L837.
- [121] Garnett J.C. Maxwell, Phil. Trans. Roy. Soc. 203 (1904) 385.
- [122] C. Miziumski, Phys. Lett. 40A (1972) 187.
- [123] J.C. Ashley, L.C. Emerson, Surf. Sci. 41 (1974) 615.
- [124] C.A. Pfeiffer, E.N. Economou, K.L. Ngai, Phys. Rev. B10 (1974) 3038.
- [125] S.S. Martinos, E.E. Economou, Phys. Rev. B24 (1981) 6908.
- [126] R.J. Warmack, R.S. Becker, V.E. Anderson, R.H. Ritchie, Y.T. Chu, J. Little, T.L. Ferrell, Phys. Rev. B29 (1984) 4375.
- [127] Y.T. Chu, R.J. Warmack, R.H. Ritchie, W. Little, R.S. Becker, T.L. Ferrell, Part. Accel. 16 (1984) 13.
- [128] M.E. Mochel, C.J. Humphreys, J.A. Eades, J.M. Mochel, A.K. Petford, Appl. Phys. Lett. 42 (1983) 392.
- [129] M. Scheinfein, A. Murray, M. Isaacson, *Ultramicroscopy* 16 (1985) 233.
- [130] J.M. Macaulay, R.M. Allen, L.M. Brown, S.D. Berger, *Microelectronic. Eng.* 9 (1989) 557.
- [131] D. De Zutter, D. De Vleeschauwer, J. Appl. Phys. 59 (1986) 4146.
- [132] J. Aizpurua, Doctoral thesis, University of Basque Country, San Sebastian, 1998.
- [133] A. Rivacoba, P. Apell, N. Zabala, Nucl. Inst. and Meth. B 96 (1995) 465.
- [134] S. Ijima, Nature 354 (1991) 56.
- [135] M.S. Dresselhaus, G. Dresselhaus, P.C. Eklund, *Science of Fullerenes and Carbon Nanotubes*, Academic, San Diego, 1996.
- [136] T. Pichler, M. Knupfer, M.S. Golden, J. Fink, Phys. Rev. Lett. 80 (1998) 4729.
- [137] R. Kuzuo, M. Terauchi, M. Tanaka, Jpn J. Appl. Phys. 31 (1992) L1484.
- [138] P.M. Ajayan, S. Ijima, T. Ichihashi, Phys. Rev. B 47 (1993) 6859.
- [139] L.A. Bursill, P.A. Stadelman, J.L. Peng, S. Praver, 49 2882, 1994.
- [140] M.F. Lin, K.W.W. Shung, Phys. Rev. B 50 (1994) 17,744.
- [141] M.F. Lin, D.S. Chuu, C.S. Huang, Y.K. Lin, K.W.W. Shung, Phys. Rev. B 53 (1996) 15,493.
- [142] C. Yannouleas, E.N. Bogachek, U. Landman, Phys. Rev. B 53 (1996) 10,225.
- [143] P. Apell, G. Mukhopadhyay, *Solid State Phys. (India)* 35C (1992) 397.
- [144] D. Östling, S.P. Apell, G. Mukhopadhyay, A. Rosén, J. Phys. B: At. Mol. Opt. Phys. 29 (1996) 5115.
- [145] B.W. Reed, J.M. Chen, M.C. MacDonald, J. Silcox, G.F. Bertsch, Phys. Rev. B 60 (1999) 5641.
- [146] J.M. Pitarke, J.B. Pendry, P.M. Echenique, Phys. Rev. B 55 (1997) 9550.
- [147] G.F. Bertsch, H. Esbensen, B.W. Reed, Phys. Rev. B 58 (1998) 14,031.
- [148] L. Dobrzynski, A.A. Maradudin, Phys. Rev. B 6 (1972) 3810.
- [149] L.C. Davis, Phys. Rev. B 14 (1976) 5523.
- [150] D. Langbein, J. Phys. A 4 (1976) 627.
- [151] R. Ruppim, Z. Phys. D 36 (1996) 69.
- [152] P. Morau, N. Brun, C.A. Walsh, C. Colliex, A. Howie, Phys. Rev. B 56 (1997) 6774.
- [153] F.J. García de Abajo, J. Aizpurua, Phys. Rev. B 56 (1997) 15,873.
- [154] J. Aizpurua, A. Howie, F.J. García de Abajo, Phys. Rev. B 60 (1999) 11,149.

- [155] D. Pines, *Elementary Excitations in Solids*, Benjamin, New York, 1964.
- [156] J. Lindhard, *Kgl. Dansk. Vid. Scls. Mat. Fys. Medd.* 28 (8) (1954).
- [157] B.I. Lundqvist, *Physik Kondens. Mat.* 6 (1967) 206.
- [158] A.W. Overhauser, *Phys. Rev. B* 3 (1971) 1888.
- [159] A.P. Stephens, Ph.D. thesis, University of Cambridge, 1987.
- [160] T.L. Ferrell, R.J. Warmack, V.E. Anderson, P.M. Echenique, *Phys. Rev. B* 35 (1987) 7365.
- [161] J.C. Maxwell, *Treatise on Electricity and Magnetism*, Dover, New York, 1891.
- [162] R. Fuchs, *Phys. Rev. A* 48 (1974) 353.
- [163] R. Fuchs, *Phys. Rev. B* 11 (1975) 1732.
- [164] F. Ouyang, M. Isaacson, *Phil. Mag. B* 60 (1989) 481.
- [165] F. Ouyang, M. Isaacson, *Ultramicroscopy* 31 (1989) 345.
- [166] J.Q. Lu, A.A. Maradudin, *Phys. Rev. B* 42 (1990) 11,159.
- [167] R. Goloskie, T. Thio, L.R. Ram-Mohan, *Comput. Phys.* 10 (1996) 477.
- [168] Z.L. Wang, J.M. Cowley, *Ultramicroscopy* 21 (1987) 335.
- [169] Z.L. Wang, J.M. Cowley, *Ultramicroscopy* 21 (1987) 347.
- [170] Z.L. Wang, J.M. Cowley, *Ultramicroscopy* 23 (1987) 97.
- [171] P. Morse, H. Feshbach, in: *Methods of Theoretical Physics*, McGraw-Hill, New York, 1953, p. 1875.